

Cepstrum-based Deconvolution Techniques for
Ultrasonic Pulse-echo Imaging of Flaws in
Composite Laminates

by

Coach K. Wei

Submitted to the Department of Civil and Environmental Engineering
in partial fulfillment of the requirements for the degree of

Master of Science

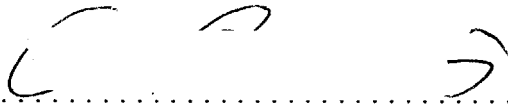
at the

MASSACHUSETTS INSTITUTE OF TECHNOLOGY

September 1998

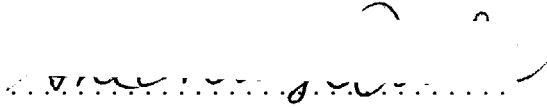
[February, 1998]

© Massachusetts Institute of Technology 1998. All rights reserved.

Author 

Department of Civil and Environmental Engineering

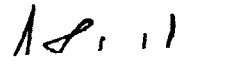
September 9, 1998

Certified by 

Shi-Chang Woo


Assistant Professor of Civil and Environmental Engineering

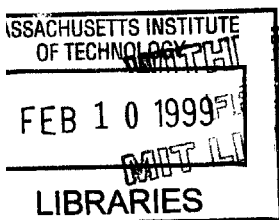
Thesis Supervisor



Accepted by 

Andrew Whittle

 Chairman, Departmental Committee on Graduate Students



Cepstrum-based Deconvolution Techniques for Ultrasonic Pulse-echo Imaging of Flaws in Composite Laminates

by

Coach K. Wei

Submitted to the Department of Civil and Environmental Engineering
on September 9, 1998, in partial fulfillment of the
requirements for the degree of
Master of Science

Abstract

Ultrasonic imaging is a powerful nondestructive evaluation (NDE) tool for flaw characterization. This thesis discusses the signal processing techniques developed for ultrasonic imaging of flaws in composite laminates. Commonly used time-domain signal processing techniques have problems including poor resolution, dependence on operator's experiences and subjectivity. Some transform-domain processing techniques, such as homomorphic deconvolution, eliminate the problems associated with traditional time-domain signal processing techniques. However, these techniques are often sensitive to environmental noise and difficult to apply under certain conditions. A modified deconvolution technique, based on homomorphic deconvolution, is proposed, which allows for processing real-life signals with noise. Results from inspecting composite laminates show clear improvement of this technique over traditional methods.

Thesis Supervisor: Shi-Chang Wooh

Title: Assistant Professor of Civil and Environmental Engineering

Acknowledgments

My sincere thanks go to Prof. Shi-Chang Wooh, my advisor. His supervision and guidance through my whole MIT years are the key driving forces that made me reach this point now. In Prof. Wooh's research Lab, NDE Lab, I fully developed my skills in a broad range of areas, such as signal processing, software, system integration and instrumentation. I feel I benefit tremendously from these experiences in my career.

I owe very much to Prof. Daniele Veneziano, my research advisor during the last year at MIT. With his help, I stepped into the area of multifractal iterated random processes and modeling of rainfall. Besides his knowledge, his sense of humor and his kindness to me are all sweet memories I would never forget.

I am also indebted to Prof. Chiang C. Mei, Prof. John R. Williams and Prof. Srinivas Devadas (Electrical Engineering) and Cynthia Stewart. Their support gave me the courage needed to work through the challenges I had during this journey.

Lots of times I really wish that I would have a chance to show my appreciation to MIT. The campus along Charles River is somehow quite disorganized, but it represents one of the most wonderful places in the world. The two years at MIT will have an enormous influence on my life.

My family and my close friends (Hey, you know your name is in this list) here at MIT deserve my greatest appreciation. Joys, sweetness, sadness and happiness are all deep in my memory. They added colors to my life here, in fact, lots of colors!

Contents

1	Introduction	8
1.1	Composite Materials	8
1.2	Ultrasonic Nondestructive Evaluation	10
1.3	Ultrasonic Imaging Techniques	13
1.4	Signal Processing Techniques	15
1.5	Motivation and Outline of Thesis	21
2	Cepstrum-Based Deconvolution Techniques	23
2.1	Theory of Homomorphic Deconvolution	23
2.1.1	Signal Model	24
2.1.2	Definition of Complex and Real Cepstrum	25
2.1.3	Homomorphic Deconvolution	27
2.2	Sensitivity Study	31
2.3	Summary	39
3	Modified Techniques for Ultrasonic Pulse-echo NDE of Layered Medium	40
3.1	Ultrasonic Pulse-echo Signals	40
3.2	Difficulties in Applying the Homomorphic Deconvolution Technique	44
3.3	Modified Deconvolution Technique	47
3.4	Summary	57
4	Ultrasonic Imaging of Composite Laminates	58
4.1	Composite Materials	59

4.2	Experimental Setup	59
4.3	Processing of A-Scans	60
4.4	Results	63
4.5	Summary	65
5	Conclusion and Future Works	69

List of Figures

1.1	Transducer arrangements: (a) pulse-echo, (b) through-transmission, and (c) pitch-catch.	12
1.2	Ultrasonic scan modes.	14
1.3	Typical signal processing techniques for B-scan imaging: (a) raw A-scan signal, (b) rectified signal, (c) video signal, (d) differentiated signal.	16
1.4	Typical A-scan waveforms, gate and threshold setup (Wooh and Daniel, 1994).	19
1.5	Bscan image resulting from a threshold of 40 (Wooh and Daniel, 1994).	20
1.6	B-scan image resulting from a threshold of 70 (Wooh and Daniel, 1994).	20
1.7	B-scan image resulting from a threshold of 100 (Wooh and Daniel, 1994).	20
2.1	General homomorphic deconvolution procedure.	28
2.2	An example of homomorphic deconvolution.	29
2.3	Basic pulse used for signal synthesis (note the deconvolved $h(n)$ is $\delta(n)$).	32
2.4	Deconvolution result when $SNR=\infty$ (note $h(t) = \delta(t) - 0.5\delta(t - 2)$). The artificially introduced time delay between the basic pulse and the echo, $t_0 = 2\mu s$, and the scaling factor, $a_0 = -0.5$, are both correctly identified.	33
2.5	Deconvolution results with different noise level: (a) $SNR=1000$. (b) $SNR=200$. (c) $SNR=100$	35
2.6	Deconvolution results with different number of echoes ($SNR=150$). (a) 1 echo. (b) 2 echoes. (c) 4 echoes.	36
2.7	Deconvolution results: effect of bandwidth.	37

2.8	Comparison of the basic pulse and rectangular pulse.	38
3.1	Ultrasonic pulse-echo experiment setup.	41
3.2	Ultrasonic wave propagation in a typical pulse-echo mode experiment.	42
3.3	Cepstrum-based deconvolution procedure showing a failure in deconvolving a typical ultrasonic pulse-echo signal.	45
3.4	Deconvolution of the same signal in Fig. 3.3 after lowpass filtering.	46
3.5	Modified cepstrum-based deconvolution procedure.	48
3.6	Creating more echoes by taking the absolute value.	49
3.7	Deconvolution result from the modified deconvolution technique.	50
3.8	Deconvolution result from the traditional deconvolution technique.	51
3.9	(a) System for homomorphic deconvolution. (b) Time-domain representation of frequency-invariant filtering.	53
3.10	Time response of frequency-invariant linear systems for deconvolution. (a) Lowpass system. (b) Highpass system. (Solid line indicates envelope of the sequence $l(t)$ as it would be applied in a DFT implementation. The dashed line indicates the periodic extension.)	53
3.11	False echoes resulted from the modified deconvolution technique.	55
3.12	Post-processing for the modified cepstrum-based deconvolution technique.	56
4.1	Schematic of a 16-ply composite laminate with Teflon patches embedded.	60
4.2	Reflection and transmission of ultrasound in material.	60
4.3	As-obtained waveforms using a transducer with a center frequency of 2.25 MHz and reconstructed signals after deconvolution for a 16-ply $[0/\pm 45/90]_{2s}$ quasi-isotropic graphite/epoxy laminate with embedded Teflon film patches: (a) Area with no embedded patches, (b) Teflon patch embedded between the 7 th and 8 th layers, (c) Teflon patch embedded between the 11 th and 12 th layers.	61

4.4	As-obtained waveforms using a focused transducer with a center frequency of 2.5 MHz and reconstructed signals after deconvolution for a 16-ply $[0/\pm 45/90]_{2s}$ quasi-isotropic graphite/epoxy laminate with embedded Teflon film patches: (a) Area with no embedded patches, (b) Teflon patches embedded between the 4 th and 5 th layers, (c) deconvolution result of the waveform shown in (a), (d) deconvolution result of the waveform shown in (b).	63
4.5	As-obtained waveforms and reconstructed signals after deconvolution for a 12-ply $[\pm 15_2/10_2]_s$ quasi-isotropic graphite/epoxy laminate with real impact damage : (a) Area with no impact, (b) area with impact damage, (c) Area with impact damage.	64
4.6	B-scan image of composite laminate with embedded Teflon patch. Time-domain processing.	66
4.7	B-scan image of composite laminate with embedded Teflon patch. Modified cepstrum-based deconvolution technique without post-processing.	67
4.8	B-scan image of composite laminate with embedded Teflon patch. Modified cepstrum-based deconvolution technique after post-processing.	68

Chapter 1

Introduction

This chapter provides the background of the thesis by an overview of composite materials and ultrasonic imaging. Composite materials are widely used in various structural systems, whose heterogeneous nature and their exposure to various environments requires new development of nondestructive evaluation (NDE) techniques. This thesis is concerned about using ultrasonics for the inspection of composite materials. Ultrasonics is one of the major NDE techniques, normally operated in either A-, B- or C-scan mode. However, ultrasonic imaging is gaining wide applications in NDE of composite laminates due to its intuitive way of presenting information. Commonly used signal processing techniques in ultrasonic imaging are within the category of time-domain or frequency-domain processing techniques. Their problems include poor resolution, dependence on operator's experiences and subjectivity. These problems bring up the demand for more advanced signal processing techniques. The last section summarizes the whole chapter and gives an outline of the thesis.

1.1 Composite Materials

Composite materials are seeing widespread use throughout aircraft structure systems and air force weapon systems. Recent years they are emerging to be the most significant material for civil engineering infrastructure design and renewal.

A structural composite is a material system consisting of two or more phases on a macroscopic scale, whose mechanical performance and properties are designed to be superior to those of the constituent materials acting independently. One of the phases is usually discontinuous, stiffer, and stronger and is called *reinforcement*, whereas the less stiff and weaker phase is continuous and is called *matrix*. Sometimes, because of chemical interaction or other processing effects, an additional phase, called *interphase*, exists between the reinforcement and the matrix. The properties of a composite material depend on the those of the constituents, geometry, and distribution of the phases (Daniel and Ishai, 1994).

Composites have unique advantages over monolithic materials, such as high strength, high stiffness, long fatigue life, low density, and adaptability to the intended function of the structure. Additional improvements can be realized in corrosion resistance, wear resistance, appearance, temperature-dependent behavior, thermal stability, thermal insulation, thermal conductivity, acoustic insulation. Furthermore, cost for acquisition and/or life cycle can be reduced through weight savings, lower tooling costs, reduced number of parts, and fewer assembly operations.

Due to the complexity of composite materials' manufacturing process, quality control during fabrication is essential to guarantee their safe applications. After fabrication, composite structures operate in a variety of thermal and moisture environments that may have a pronounced impact on their performance. These hygrothermal effects are a result of the temperature and moisture content variations and are related to the difference in thermal and hygric properties of the constituents. Service-induced damage growth, such as damage due to impact loading (Daniel and Wooh, 1990; Finn, He and Springer, 1993), must be timely evaluated to prevent potential failure.

Composites present several specific challenges to nondestructive evaluation. Firstly, major defects such as debris, inclusions, delaminations and impact damage must be revealed. Secondly, inspections must reveal defect states such as high void content, fiber bunching, resin richness and ply misorientations. Thirdly, composites need to be evaluated for subtle deficiencies such as those due to diffused flaw populations, microporosity, matrix crazing, fiber breakage, undercure, poor quality fiber/matrix

bonding and poor quality adhesive or interlaminar bonding. Various NDE methods have been used for inspecting composites, including radiographic method, acoustic emission, thermal methods, optical methods, vibration techniques, chemical spectroscopy, computed tomography, eddy-current testing, ultrasonic methods, electrical and magnetic testing, dielectrometry and microwave techniques. In general, each method displays its advantages and disadvantages over others. Ultrasonic NDE, as a quantitative approach, is of particular interest and also one of the most widely used methods for NDE of composites (Chang, Couchman and Yew, 1971; Wooh and Daniel, 1994).

1.2 Ultrasonic Nondestructive Evaluation

Nondestructive evaluation (NDE) is concerned with identifying, locating and characterizing structural properties and/or defects in a nondestructive fashion. NDE plays an important role in the life cycle of an engineering structural system (Wooh, 1995). The following list includes the mainstream inspection and monitoring methods currently employed, based primarily on the physical principles of operation:

- Visual/Optical Testing (VT)
- Liquid Penetrant Testing (PT)
- Magnetic Particle Inspection (MPI)
- Eddy Current (EC)
- Radiographic Testing (RT)
- Acoustic Emission (AE)
- Ultrasonic Testing (UT)

Ultrasound technology is one of the most employed methods for NDE. Ultrasonic waves are mechanical waves oscillating at a frequency beyond 20 kHz, which are often generated by exploiting piezoelectric effect. Electrical pulses excite a piezoelectric

material (transducer), generating stress waves which are emitted into an object at frequencies in the range of 30 kHz to 50 MHz and higher, depending on the application. Interaction of these waves with the material results in the returning of some portion of energy to a receiver, which is further converted into electrical energy through the piezoelectric effect. The signals contain useful information about the inspected material, which could be extracted by using signal processing techniques.

Ultrasonic NDE is widely used for quantitative flaw characterization by determining the location, size and orientation of flaws. In the followings, basic operating modes of ultrasonic testing are introduced first. Then, ultrasonic flaw characterization methods are discussed. Discussion of ultrasonic imaging techniques is left for the next section for a more detailed description.

Basic Operating Modes

Typically, ultrasonic transducers are set up in one of the three fashions: pulse-echo, through-transmission, and pitch-catch. These techniques are the basic configurations which can lead to more sophisticated modes, as illustrated in Fig. 1.1. A single transducer operating as both transmitter and receiver, as shown in Fig. 1.1(a), emits an ultrasonic signal which is reflected off the backwall of the material and received by the same transducer. This configuration is called *pulse-echo*, which is often used when inspection is limited to a single side (i.e., single-sided access). If a pair of transducers are placed on opposite sides of the medium, one as a transmitter and the other one as a receiver (Fig. 1.1(b)), the pulse is said to be sent in *through-transmission*. In the through-transmission mode, transmitter and receiver are physically and electrically isolated, which introduces clean signals and high signal-to-noise ratios. Therefore, this mode is often preferred over pulse-echo, if both sides of the testing material are accessible.

Two transducers situated on the same surface can be used in *pitch-catch* mode, again in a transmitter-receiver setup, as shown in Fig. 1.1(c). The transmitter sends an oblique beam into the specimen which will be reflected off the opposite side and be caught by the receiver.

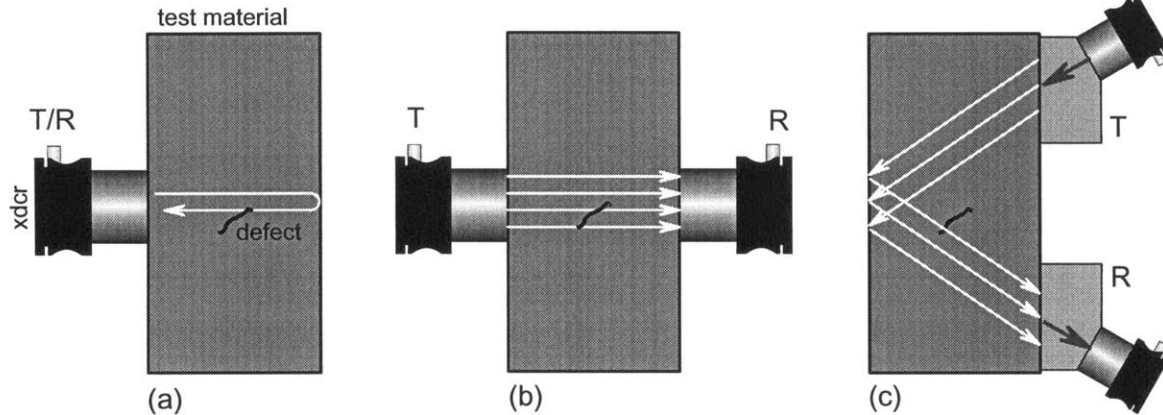


Figure 1.1: Transducer arrangements: (a) pulse-echo, (b) through-transmission, and (c) pitch-catch.

Although the transducers shown in Fig. 1.1 are in direct contact with the solid through the use of a couplant, all of these methods may easily be extended to non-contact applications involving a fluid surrounding the specimen.

A-scan

The most fundamental form of information obtained from ultrasonic inspection is the so-called *A*-scan, which contains rich information about the material and flaws. The *A*-scans are obtained by repetitively transmitting pulses into a material, and synchronizing an oscilloscope to the transmitted bursts. If the transmitting transducer is simultaneously used as a receiver (pulse-echo mode), then the echoes will appear on the screen. The horizontal axis gives time information (this correlates to time-of-flight) while the vertical axis indicates the echo amplitude. Careful analysis and interpretation of the echoes on the display screen can provide information about the extent of damage in the material. The *A*-scan can provide through-thickness information at a point.

Interpretation of the *A*-scan can lead to quantitative methods to determine certain characteristics, such as its location, size, depth, height, and orientation. This information is critical in assessing the condition of the structure and safeguarding it from potential failure. However, interpretation of the *A*-scan waveform requires both

experiences and knowledge in NDE. Thus, the need for well-trained personnel who are skilled in calibrating the instrumentation and interpreting signals limits the wide application of ultrasonic NDE. Ultrasonic imaging exhibits a major improvement here. Presenting information in the form of an image is one of the most intuitive ways to understand, which dramatically reduces the difficulty of data interpretation. This topic will be talked in the next section.

1.3 Ultrasonic Imaging Techniques

Ultrasonic imaging is capable of displaying cross-sectional, planar and full volumetric images of virtually any conceivable material or component using immersion testing. Typically images are categorized into *B*-scans and *C*-scans, which are obtained by scanning and processing the *A*-scans at each point (Krautkämmer and Krautkämmer, 1990).

B-scan images represent cross-sectional views of defects in the material along a scan line. Using a normal incident ultrasonic beam, a distance between interfaces can be accurately determined by measuring the time interval between the echoes reflected from the interfaces. By processing a series of *A*-scans along a line of interest and by mapping the amplitude-time information into pixel information, a cross-sectional (*B*-scan) image can be constructed. Figure 1.2 shows schematically the *B*-scanning procedure.

An image obtained by scanning over an plane is called *C*-scan, representing a planar view of the material and flaws. In order to provide excellent spatial resolution, a focused transducer is usually used for scanning. In general, intensity or echo amplitudes are mapped into brightness of the image while the transducer scans the area of interest on the specimen in a raster fashion, as shown in Fig. 1.2. Since the backface reflection represents the signal loss due to material attenuation and reflection from flaws (if they exist) along the path of ultrasonic wave propagation at each point, gated peak amplitude of backface reflection is often used to construct an image.

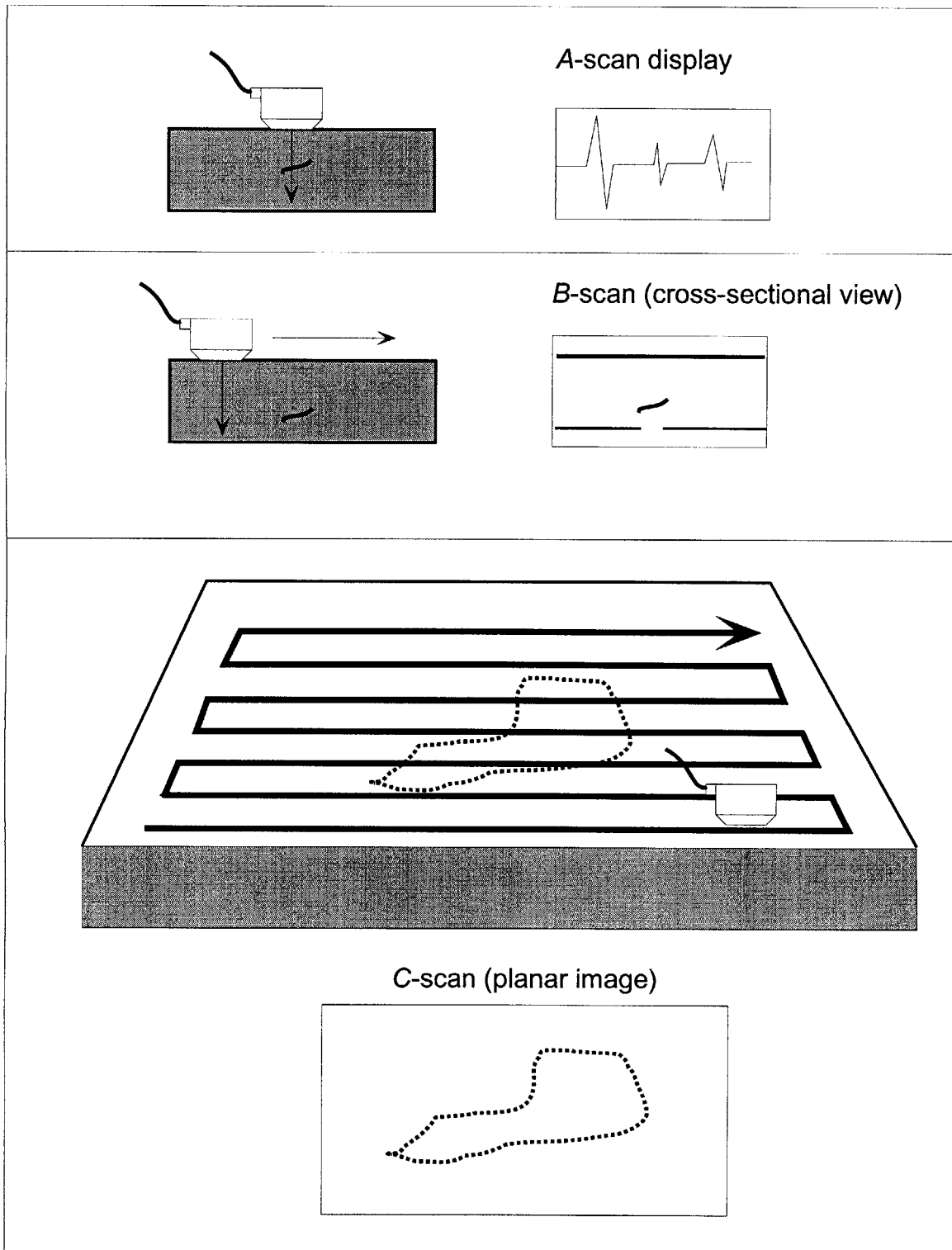


Figure 1.2: Ultrasonic scan modes.

These *B*- and *C*- scans are often performed in an immersion tank. Immersion offers several advantages comparing with direct contact testing. An aqueous environment results in the minimum wear of the transducer and forms a uniform and even coupling medium between test material and transducer. Also, the creation of transverse waves due to refraction at the transducer/fluid interface can be avoided since fluids can only sustain longitudinal waves (Krautkamer and Krautkamer, 1990).

1.4 Signal Processing Techniques

Typically, B-scan and C-scan images are obtained by processing the acquired A-scan waveforms (RF signals) in the time domain. For normal incident pulse-echo mode, the time scale is proportional to the distance from the specimen surface in the thickness direction. Thus, it is possible to map the RF signals into a B-scan image by scanning along a line parallel to the specimen surface. The waveforms acquired during the scanning are interrogated on a point-by-point basis and transformed into a format suitable for B-scan imaging. The as-obtained records have an oscillatory shape whose peaks vary between positive and negative values, as illustrated in Fig. 1.3(a). An image consists of only positive discrete numbers representing gray scale or intensity at a point. Thus, the raw RF signals are not suitable for imaging purposes and some signal processing techniques must be applied.

One simple processing technique is the so-called *rectification*. This technique maps the absolute values of the RF signal into grayscales, as shown in Fig. 1.3(b). However, this approach is not correct because a single pulse is taken into a series of narrow signals of various amplitudes, as shown in Fig. 1.3(b). A single interface in the material, corresponding to a single pulse in the RF signal, is shown as a series of interfaces with various intensity in the resulting image.

Another processing technique, which is often found in medical diagnostics equipment, is illustrated in Fig. 1.3(c). A single pulse is transformed into a video signal by displaying only the envelope of the positive components. By doing this, a single interface in the material can be represented as a single interface in the obtained im-

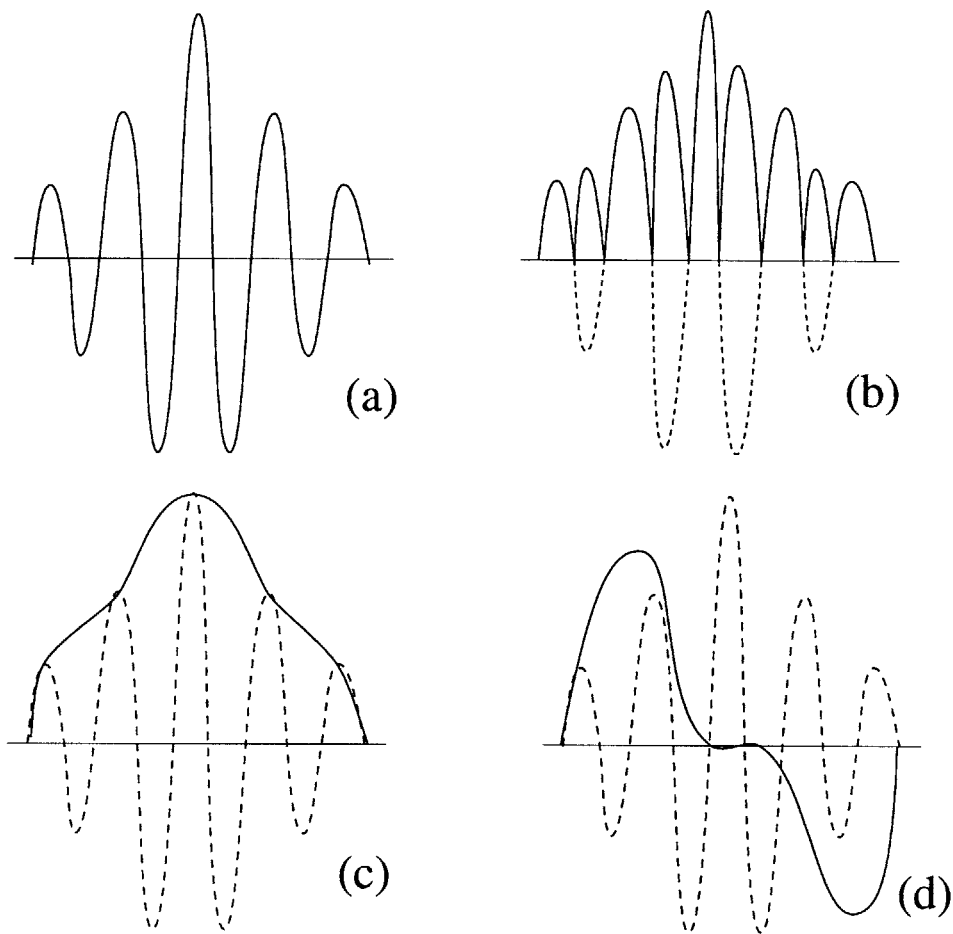


Figure 1.3: Typical signal processing techniques for B-scan imaging: (a) raw A-scan signal, (b) rectified signal, (c) video signal, (d) differentiated signal.

age, which is correct. The disadvantage of this approach is its poor resolution. If the distance between two interfaces are not far enough, the echoes from these interfaces will be mixed together in the RF signal and thus could not be differentiated by this technique.

The other processing technique, which is mostly commonly used in NDE, is by using a gate and setting a threshold. By setting up a gate, which is actually a time window, only the signal inside the gate is processed for imaging and signals outside the window are simply abandoned. Signals whose magnitude smaller than the predetermined threshold value are taken as zero and only those signals whose magnitude exceeds the threshold are mapped into an image. The fourth technique is called *differentiated signal*, which displays the differentiation of the video signal. This has the advantage of enhancing the amplitude resulting in better reproducible measurements in the time domain. The overall duration of a pulse, however, does not change significantly (Wooh and Daniel, 1994).

Figure 1.4 shows typical A-scan waveforms and locations of gates and threshold setups. Figure 1.4(a) shows an A-scan in an undamaged region, in which the first echo represents the front face reflection and the one that appears in the gate 2-3 is the backface reflection. Figure 1.4 (b) indicates two delaminations in the middle of the material, one below the other. The latter has a smaller amplitude because of the shadow effect caused by the first delamination. Figure 1.4 (c) shows reflections reflected from a delamination located very close to the front surface. Gate 1-2, which opens at line 1 and closes at line 2, is set to image the cross-section of the material. Gate 2-3, which opens at line 2 and ends at line 3, is used to image the backwall. Two threshold values are chosen: -80 and -180 (arbitrary unit). The problem associated with this method is the subjectiveness in selecting the threshold and gate location. For example, by choosing a threshold of -160, only one delamination is detected in Fig. 1.4(b). Only a threshold around -80 could identify the second delamination correctly. So, a proper selection of the threshold value is the key to successful imaging. There is no theory guiding the selection of threshold value and it is totally dependent on the operator's experience and knowledge in the area. Figures 1.5, 1.6, and 1.7

show the influence of threshold on the image quality. Improper selection of threshold may result in faulty images as shown.

Another problem of this processing technique is its poor resolution. In Fig. 1.4(c), the echoes returned from the front face and the flaw are not separated in the waveform, which means that it is impossible for this time-domain signal processing technique to differentiate the flaw from the frontface. Thus the resolution is limited by the duration of the echo itself, since this technique can only differentiate well-separated echoes.

Drifting of the waveform also causes problems. In general, the waveforms drift back and forth in the time axis at different locations because of surface irregularities or trigger sensitivity of the digitizer. Therefore, for each waveform, the absolute gate opening positions in the array should be calculated by the given relative offset from the front surface reflection rather than by explicitly specified absolute indexes. This adds additional complexity to the hardware system and software system and causes the need for the so-called *surface follower mode*.

The signals can be also processed in the frequency-domain. One method is to measure the frequency spacing of the resonance peaks in the magnitude spectrum (Chang *et al.*(1974)). This frequency spacing has a certain relationship with the time-of-flight (TOF) of the echoes and thus the TOF can be determined from the measured frequency spacing. The problem associated with this technique is that it is difficult to automate and requires human interaction. Another technique that has been used by Kinra and Dayal (1988), Iyer and Kinra (1991a, 1991b), Pialucha *et al.* (1989) and other researchers is to obtain the spectrum of the system transfer function and further the TOF information by subtracting the spectrum of the reference pulse from the spectrum of the received waveform. These techniques require an *a priori* knowledge of the reference pulse and a very stable experimental condition that ensures the repeatability of the reference pulse. Comparing with the time-domain techniques, frequency domain techniques don't require the echoes to be separated in time-domain. But they still have limitations that make their applications difficult in some situations.

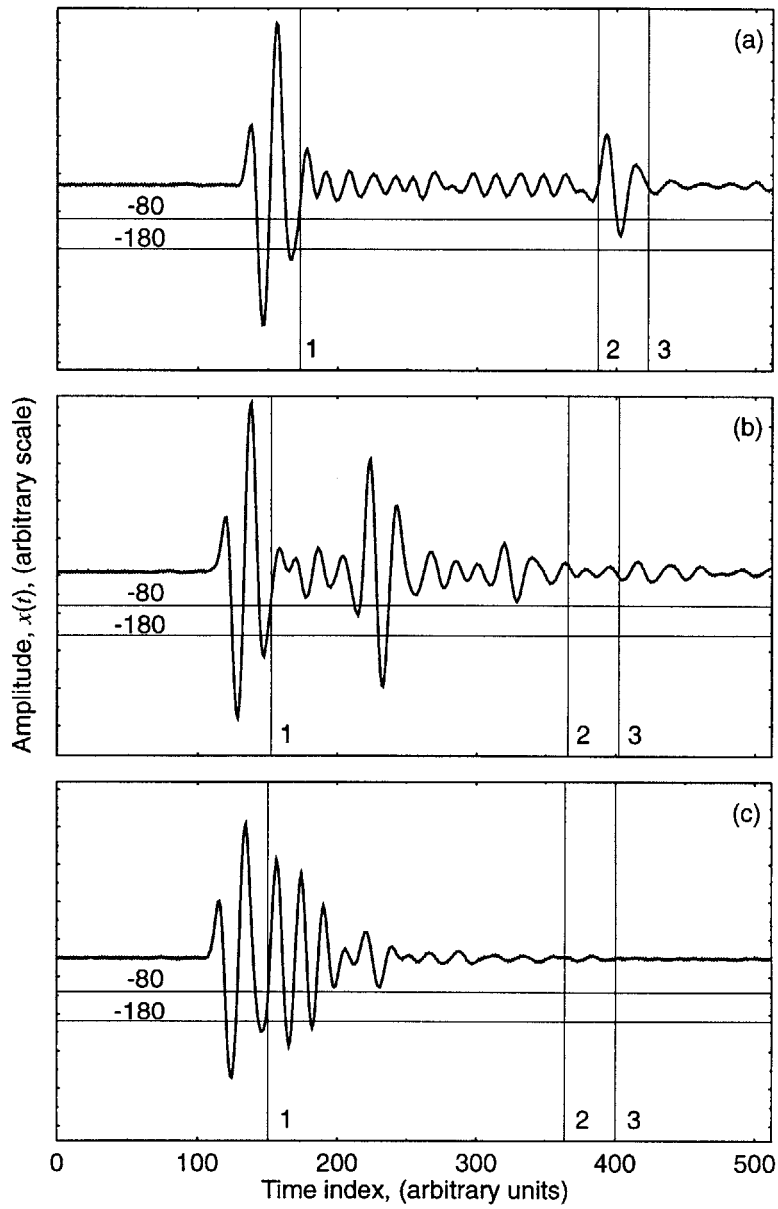


Figure 1.4: Typical A-scan waveforms, gate and threshold setup (Wooh and Daniel, 1994).

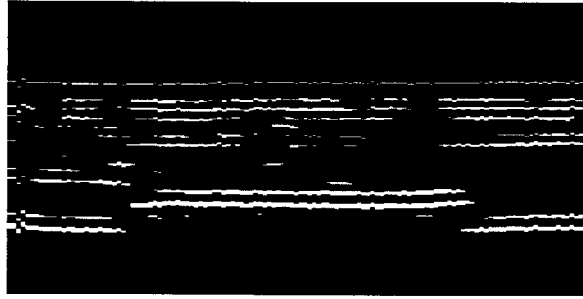


Figure 1.5: Bscan image resulting from a threshold of 40 (Wooh and Daniel, 1994).

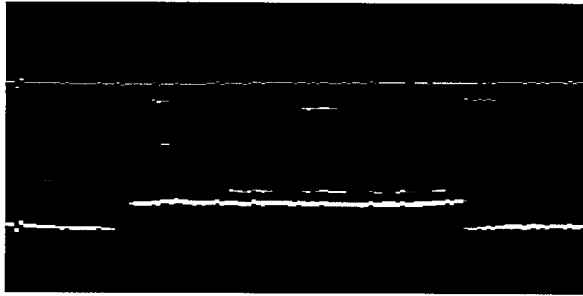


Figure 1.6: B-scan image resulting from a threshold of 70 (Wooh and Daniel, 1994).

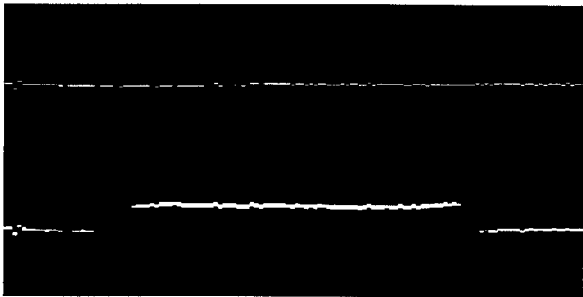


Figure 1.7: B-scan image resulting from a threshold of 100 (Wooh and Daniel, 1994).

In summary, while processing A-scan waveforms could result in B-scan or C-scan images, which are much more intuitive for flaw detection, all the above processing techniques have some serious drawbacks. The signal processing technique to enhance the quality of ultrasonic images remains an ongoing research topic.

1.5 Motivation and Outline of Thesis

Ultrasonic NDE is a powerful technique for flaw characterization in many applications. The basic modes of operation are: pulse-echo, through-transmission, and pitch-catch. By using these methods, it is possible to determine the size, location and orientation of flaws by processing the obtained A-scan waveforms. Data interpretation here is crucial for the successful application of ultrasonic NDE.

However, sufficient experiences and knowledge in NDE is required for data interpretation. The need of well-trained personnel for operation somehow limits the application of ultrasonic NDE. In this sense, ultrasonic imaging provides a much more intuitive way for presenting information. Grayscale or color images can be easily used to determine size, location and orientation of flaws, which may reduce the need of skilled personnel.

B-scan and C-scan are mostly used imaging methods. The first provides an image of a cross-section while the latter provides a planar view of the material. They are obtained through scanning and processing of the obtained A-scan waveforms.

The current implementations are mostly based on time-domain processing. While they have been successfully applied, they have many drawbacks. The resolution is limited by the duration of the echo; the selection of time window (gate) is subjective; the choice of amplitude threshold is also subjective. Frequency-domain signal processing techniques offer some comparative advantages. But they require either human interaction, *apriori* knowledge or stable testing conditions. The existence of these problems necessitates the need for new and robust signal processing techniques. This thesis is targeted for the research on this problem.

The thesis will first introduce a useful echo detection technique, homomorphic deconvolution. This technique gives good result if the signal is free from noise. But the sensitivity of this technique hinders its application in ultrasonic imaging. After a sensitivity analysis of homomorphic deconvolution, a modified cepstrum-based deconvolution technique is proposed. This technique overcomes the extreme sensitivity to noise and makes using deconvolution techniques for ultrasonic imaging feasible. Following the discussion of this proposed technique, an application of the technique to ultrasonic imaging of composite laminates is presented. Conclusion and future works are presented in the last chapter.

Chapter 2

Cepstrum-Based Deconvolution

Techniques

This chapter provides the basic theory of cepstrum-based deconvolution techniques. *Homomorphic deconvolution*, an excellent solution for some of the signal processing problems in ultrasonic NDE, is introduced first. The major mode of difficulties in applying this theory resides in its sensitivity to noise. To this end, a sensitivity study based on numerical experiments is performed. Unfortunately, in ultrasonic NDE, most of the signals contain certain level of noise due to various reasons, which deters the application of this deconvolution technique. The study in this chapter is the foundation for the proposed signal processing technique for ultrasonic pulse-echo imaging, which will be discussed in the next chapter.

2.1 Theory of Homomorphic Deconvolution

The concept of cepstrum was introduced by a paper titled *The Quefreny Analysis of Time Series for Echoes: Cepstrum, Pseudoautocovariance, Cross-Cepstrum and Saphe Cracking* by Bogert, Healy and Tukey (1963). They observed that the logarithms of the power spectrum of a signal containing an echo has an additive periodic component due to the echo, and thus the Fourier transform of the logarithm of the power spectrum should exhibit a peak at the echo delay. They called this function the

cepstrum. At about the same time, Oppenheim (1969) proposed a new class of systems called *homomorphic systems*. The transformation of a signal into its cepstrum is a homomorphic transformation. Since then, the concepts of the cepstrum and homomorphic systems have proved useful in signal analysis and have been applied with success in speech signal processing (Oppenheim, 1969; Schafer and Rabiner, 1970), seismic signals (Ulrych, 1971; Tribolet, 1979), biomedical signals (Senmoto and Childers, 1972) and sonar signals (Reut *et al.*, 1985). Here we will introduce the theory and its possible application in ultrasonic NDE.

2.1.1 Signal Model

Assume $y(t)$ is the signal under investigation and furthermore we assume that $y(t)$ is a convolution of two components, $x(t)$ and $h(t)$. In other words, we consider our signal model to be:

$$y(t) = x(t) * h(t) , \quad (2.1)$$

in which $h(t)$ is the impulse response function of the system. We assume $h(t)$ is composed of a series of spikes that could be approximated as

$$h(t) = \sum_{i=0}^N a_i \delta(t - t_i) \quad (2.2)$$

where $\delta(t)$ is a delta function:

$$\delta(t) = \begin{cases} \infty, & t = 0 \\ 0, & \text{otherwise} \end{cases}$$

This is a typical echo-detection model, which simply says $y(t)$ is composed of $x(t)$ and its echoes. This kind of model is very useful and widely seen in the aforementioned signal processing areas. We will show that this model can also be applied to the ultrasonic pulse-echo signals. Typically, $y(t)$ is a known signal, and $x(t)$ and $h(t)$ are

both unknown. But we know that $h(t)$ is composed of a series of spikes, as expressed by eq. (2.2). The question is how to obtain $h(t)$, which is our point of interest. If we take $y(t)$ as the output of the system, and $x(t)$ as the input, then $h(t)$ is the response function of the system. The problem is how to obtain the system function while only the output known. In other words, we are interested in deconvolving $x(t)$ and $h(t)$ so that we could obtain $h(t)$. This is a deconvolution problem.

Today signals are mostly processed in the discrete-time domain. Typically, a continuous analog signal, say $x(t)$, is sampled at a period of T , the so-called *sampling period*, and quantized at a resolution of 8 to 16 bits. Considering discretization, the signal is modeled equivalently as:

$$y(n) = x(n) * h(n) , \quad (2.3)$$

where n is the time index and the time $t = nT$. Similarly, $h(n)$ is the corresponding impulse response function of the system, which is assumed to be a series of spikes approximated as

$$h(n) = \sum_{i=0}^{N-1} a_i \delta(n - n_i) . \quad (2.4)$$

For the sake of simplicity, we will take this discrete signal model as our basic model in the following discussions.

2.1.2 Definition of Complex and Real Cepstrum

Suppose $X(\omega)$ is the *Fourier* transform of a stable signal $x(t)$, $X(\omega)$ could be expressed in polar form as:

$$X(\omega) = |X(\omega)| \exp[j \arg(X(\omega))] , \quad (2.5)$$

where $|X(\omega)|$ and $\arg(X(\omega))$ are the respective magnitude and angle of the complex number $X(\omega)$, ω is the frequency and j is a pure imaginary number as the square root of -1 .

The complex cepstrum of $x(n)$ is defined to be a stable signal $\bar{x}(n)$ whose Fourier transform is

$$\bar{X}(\omega) = \log[X(\omega)] . \quad (2.6)$$

Normally the natural logarithm is used, which will be assumed throughout this thesis, although any base could be used for the logarithm. The logarithm of a complex number $X(\omega)$ is defined as:

$$\log[X(\omega)] = \log[|X(\omega)|] + j\arg(X(\omega)) . \quad (2.7)$$

However, the imaginary part of eq. (2.7) is not well defined yet since the angle for complex number is only unique within integer multiples of 2π . For further discussion of this definition, refer to Oppenheim and Schaffer (1991). Some important properties of complex cepstrum are outlined as follows:

- Property 1: The complex cepstrum decays at least as fast as $\frac{1}{|n|}$.
- Property 2: $\bar{x}(n)$ will have infinite duration, even if $x(t)$ has finite duration.
- Property 3: If $x(n)$ is real, then $\bar{x}(n)$ is also real.

Besides the complex cepstrum, the real cepstrum $c_x(n)$ is defined as the inverse transform of the logarithms of the magnitude of the Fourier transform:

$$c_x(n) = \frac{1}{2\pi} \int_{-\pi}^{\pi} \log |X(\omega)| \exp(j\omega nT) d\omega . \quad (2.8)$$

The relationship between the real cepstrum $c_x(n)$ and the complex cepstrum $\bar{x}(n)$ can be shown as:

$$c_x(n) = \frac{\bar{x}(n) + \bar{x}^*(-n)}{2} . \quad (2.9)$$

Compared to the real cepstrum, the complex cepstrum reserves all the information and original signal $x(n)$ could be fully recovered from the complex cepstrum. But the complex cepstrum is much more difficult to compute, since it involves not only the magnitude of the Fourier transform but also the angle. The real cepstrum is, on the other side, easier to compute but it is not invertible.

2.1.3 Homomorphic Deconvolution

For a system of input $x(n)$ and output $y(n)$ such as

$$y(n) = x(n) * h(n) ,$$

Fourier transform of the above equation can be written as:

$$Y(\omega) = X(\omega)H(\omega) , \quad (2.10)$$

where $Y(\omega)$, $X(\omega)$, and $H(\omega)$ are the respective frequency representations of $y(n)$, $x(n)$, and $h(n)$. As a result, convolution in the time domain becomes multiplication in the frequency domain. By further taking a logarithm operation of eq. (2.10), we obtain:

$$\log[Y(\omega)] = \log[X(\omega)] + \log[H(\omega)] . \quad (2.11)$$

Taking an inverse Fourier transform, the following equation relating the complex ceptra $\bar{y}(n)$, $\bar{x}(n)$, and $\bar{h}(n)$ holds:

$$\bar{y}(n) = \bar{x}(n) + \bar{h}(n) , \quad (2.12)$$

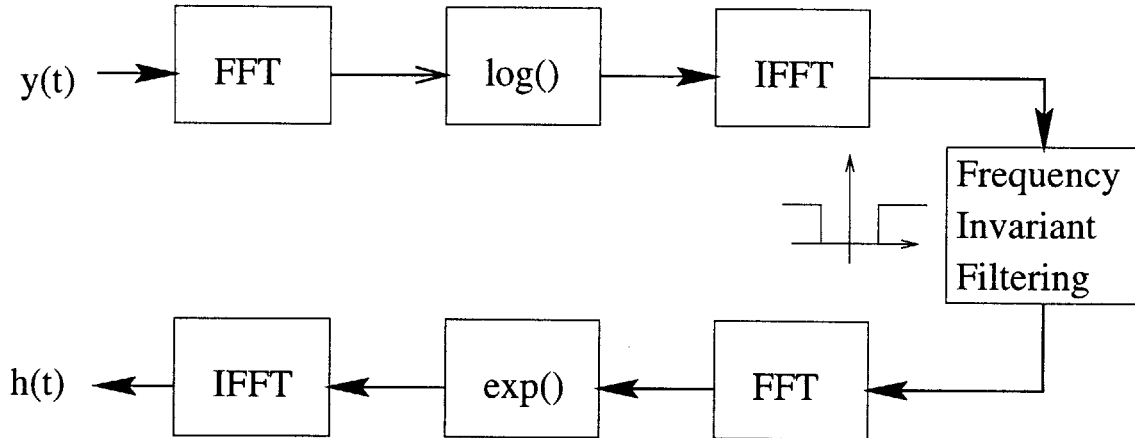


Figure 2.1: General homomorphic deconvolution procedure.

Now we are in the so-called *quefrequency* domain. Suppose $\bar{x}(n)$ and $\bar{h}(n)$ are separable in this domain, we could remove $\bar{x}(n)$ from $\bar{y}(n)$, and then obtain the complex cepstrum of $h(n)$ and correspondingly recover $h(n)$.

Extraction of $\bar{h}(n)$ from $\bar{y}(n)$ is commonly accomplished by the so-called *frequency-invariant filtering*, in which $\bar{h}(n)$ is approximately taken as (for simplicity, we will use '=' in the following equation instead of ' \approx '):

$$\bar{h}(n) = l(n)\bar{y}(n), \quad (2.13)$$

where $l(n)$ is a frequency-invariant filter. Suppose that $\bar{x}(n) = 0$ for $n > n_0$ and $\bar{h}(n) = 0$ for $n < n_0$, then a *frequency-invariant linear filter* such as

$$l(n) = \begin{cases} 0, & \text{for } n < n_0 \\ 1, & \text{for } n \geq n_0 \end{cases}$$

will remove $\bar{x}(n)$ from $\bar{y}(n)$ and thus recover $\bar{h}(n)$.

The problem in question is whether $\bar{x}(n)$ and $\bar{h}(n)$ are separable. Theory shows that, according to Property 1, $\bar{x}(n)$ decays at least as fast as $\frac{1}{|n|}$. So most of the energy associated with $x(n)$ should be concentrated in the narrow band centered

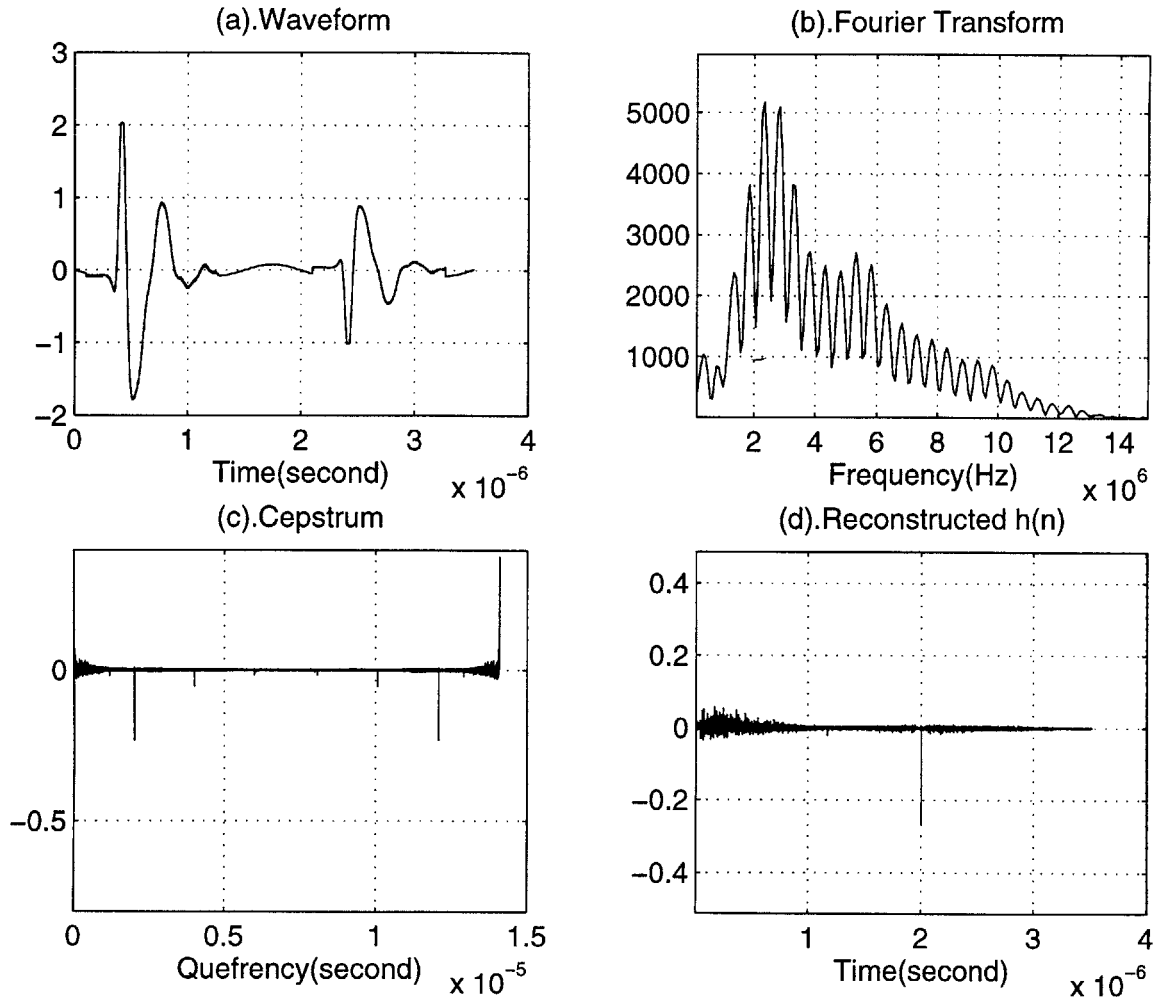


Figure 2.2: An example of homomorphic deconvolution.

around zero in the *queffrequency* domain. On the other hand, it could also be shown that $\bar{h}(n)$, if $h(n)$ has the expression of eq. (2.2), will stand out in the area away from 0 in the *queffrequency* domain. The different characteristics of the two kinds of signals make the separation in the *queffrequency* domain possible.

After extracting $\bar{h}(n)$ from $\bar{y}(n)$, $h(n)$ can be reconstructed from $\bar{h}(n)$ by taking the inverse of the operations done so far. In summary, the homomorphic deconvolution procedure is shown in Fig. 2.1. An example of using this technique to deconvolve a signal is shown in Fig. 2.2. Figure 2.2(a) to 2.2(d) respectively show the as-obtained waveform, the magnitude of Fourier transform, the real cepstrum of the signal and the deconvolved signal $h(n)$. An echo located at $t = 2 \mu\text{s}$ is clearly and precisely identified

in the deconvolved signal. Also, the echo has a negative polarity and its amplitude is approximately 0.3 according to $h(n)$. In the deconvolution, a frequency-invariant high-pass filter was used.

2.2 Sensitivity Study

This section introduces numerical studies of the cepstrum-based homomorphic deconvolution. As shown in the example in the previous section, this technique seems to be an excellent tool that deconvolves signals blindly. It is shown in Fig. 2.2 that the time-of-flight of the echo can be precisely and clearly identified. However, this deconvolution technique is very sensitive to noise. In application to ultrasonic pulse-echo signals, this technique failed for most of the signals we acquired. To understand the possible factors influencing the deconvolution result, a sensitivity study is executed based on numerical experiments. According to the need in ultrasonic signal processing, the following three factors are considered in the numerical studies:

- Signal-to-noise Ratio(SNR)
- Bandwidth
- Number of echoes contained in the signal

In the following experiments, all the signals used are artificially synthesized by using a basic pulse, $x(n)$. This basic pulse is truncated from an ultrasonic pulse-echo experimental waveform. The shape of the pulse and its spectrum are shown in Fig. 2.3. Each signal, denoted by $y(n)$, which is actually used for the numerical experiment, is synthesized by scaling the basic pulse, namely multiplying $x(n)$ by a constant α_i ($-1 < \alpha_i < 1$), shifting the scaled basic pulse by a certain time delay t_i (or, using time index, $n_i = \frac{t_i}{T}$, T is the sampling period). This scaled and shifted pulse is denoted by $\alpha_i x(n - n_i)$. This procedure may be repeated several times to create several echoes. The signal $y(n)$ is obtained by adding together the basic pulse $x(n)$ and these shifted and scaled versions, $\alpha_i x(n - n_i)$, $i = 0, \dots, N - 1$. Following this procedure, we get

$$h(n) = \sum_{i=0}^{N-1} a_i \delta(n - n_i) ,$$

with all the known parameters, a_i and n_i .

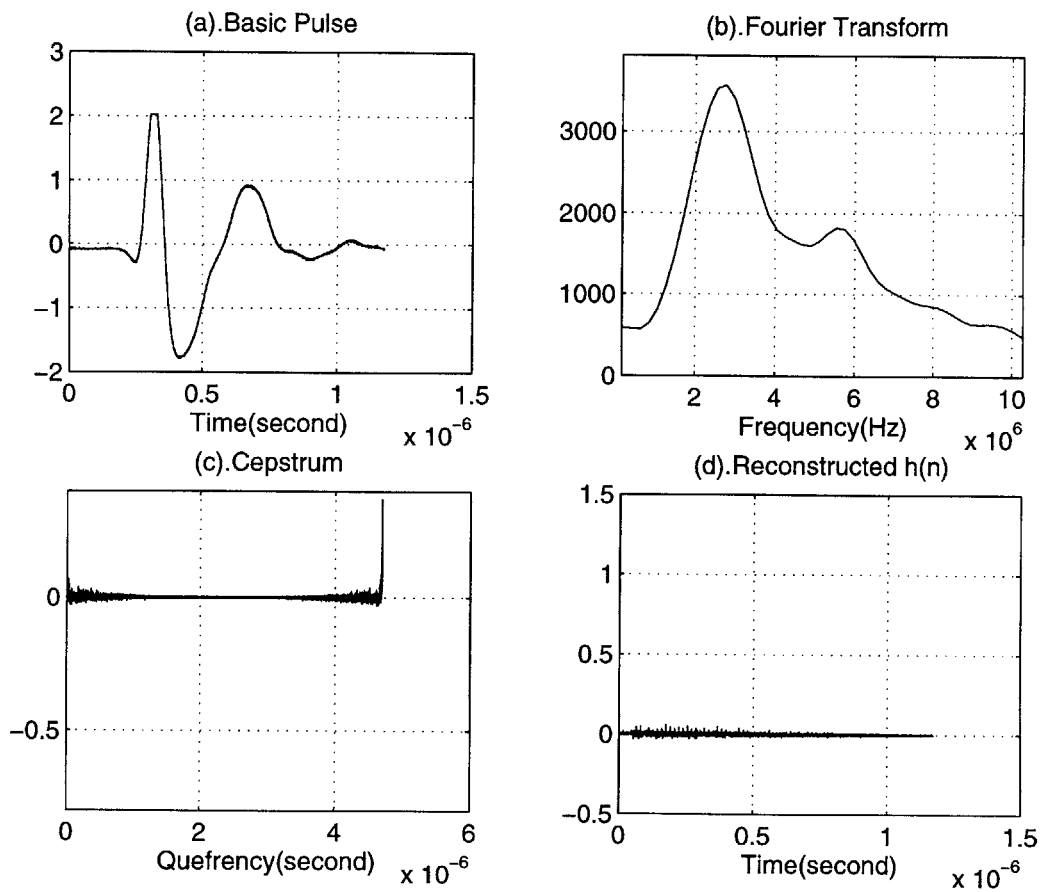


Figure 2.3: Basic pulse used for signal synthesis (note the deconvolved $h(n)$ is $\delta(n)$).

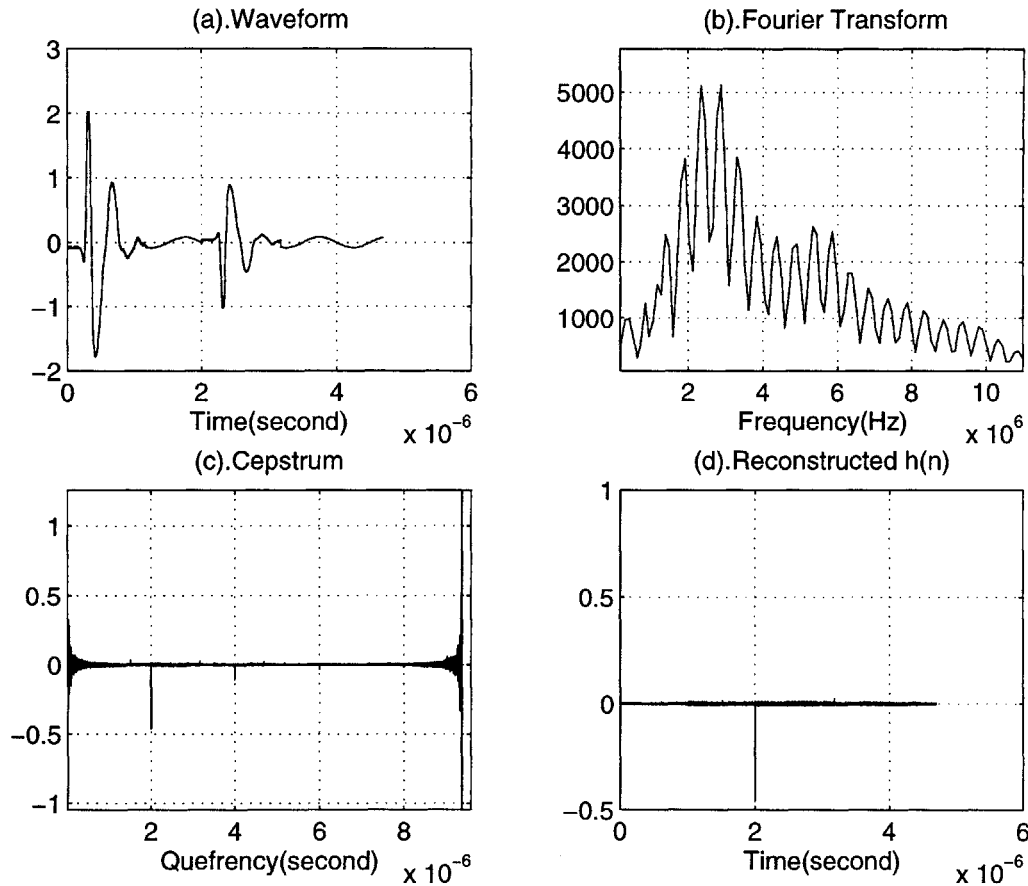


Figure 2.4: Deconvolution result when $\text{SNR}=\infty$ (note $h(t) = \delta(t) - 0.5\delta(t - 2)$). The artificially introduced time delay between the basic pulse and the echo, $t_0 = 2\mu\text{s}$, and the scaling factor, $a_0 = -0.5$, are both correctly identified.

Signal-to-Noise Ratio

Figure 2.4 shows the deconvolution result when $\text{SNR} \rightarrow \infty$ (i.e., no additive noise). The synthesized signal, $y(t)$, is obtained by adding up the basic pulse and a scaled, shifted version of the basic pulse, with a scaling factor of -0.5 and a time delay of $2 \mu\text{s}$. This implies that $h(t) = \delta(t) - 0.5\delta(t - 2)$. The signal-to-noise ratio is considered to be ∞ , since no noise is introduced due to the fact that $y(t)$ is precisely modeled by $y(t) = x(t) * h(t)$ with $h(t) = \delta(t) - 0.5\delta(t - 2)$. The deconvolution result is almost perfect in the sense that the acquired $h(n)$ matches the theoretical $h(t) = \delta(t) - 0.5\delta(t - 2)$ extremely well.

The result shown in Fig. 2.4 seems to indicate great promise of applying this deconvolution technique to real experimental data. However, a further study, by adding random white noise to synthesized signals, shows extreme sensitivity of the technique to noise. Figure 2.5 shows the effect of increasing noise level. Signals used in this figure are similar to those used in Fig. 2.4, except for having a certain amount of white noise added. They are generated using the following formula, where $x(t)$ is the basic pulse:

$$y(t) = x(t) - 0.5x(t - 2) + \beta w(t) ,$$

which implies $h(t) = \delta(t) - 0.5\delta(t - 2)$ as in Fig. 2.4. The only difference is the inclusion of the additive noise, $\beta w(t)$. White noise denoted by $w(t)$ has an amplitude between -1 and 1 . The parameter β is used for controlling the signal-to-noise ratio. The signal-to-noise ratio (SNR) is defined as the ratio between the maximum value of the basic pulse $x(t)$ and the maximum of the additive noise $\beta w(t)$. In Fig. 2.5, a SNR of 1000, 200 and 100 are used for signals (a), (b) and (c), respectively. The simulated signals are shown on the top of the figures while the deconvolved results are shown at the bottom of the figures. For SNR = 1000, deconvolution still gives a very good estimation of $h(t)$, as shown in Fig. 2.5 (a). The time delay of the echo is precisely identified but the estimation of the scaling factor, a_0 , is slightly degraded, compared to SNR = ∞ in Fig. 2.4. With a SNR = 200, in Fig. 2.5 (b), the time delay is still correctly identified but the estimation of the scaling factor, a_0 , is further degenerated. When the noise level is raised to a SNR = 100, the estimation of $h(t)$ from deconvolution is close to a failure, as shown in Fig. 2.5 (c).

Although homomorphic deconvolution gives excellent echo detection when the signal is clean, it fails with even a very low noise level. In Fig. 2.5 (c), noise is only one percent of the signal and the signal does not look much degraded from that of Fig. 2.5(a). The failure of homomorphic deconvolution in this case implies the extreme sensitivity of this technique. Unfortunately, it is likely that most of the ultrasonic pulse-echo signals have at least this amount of noise, which deters the direct

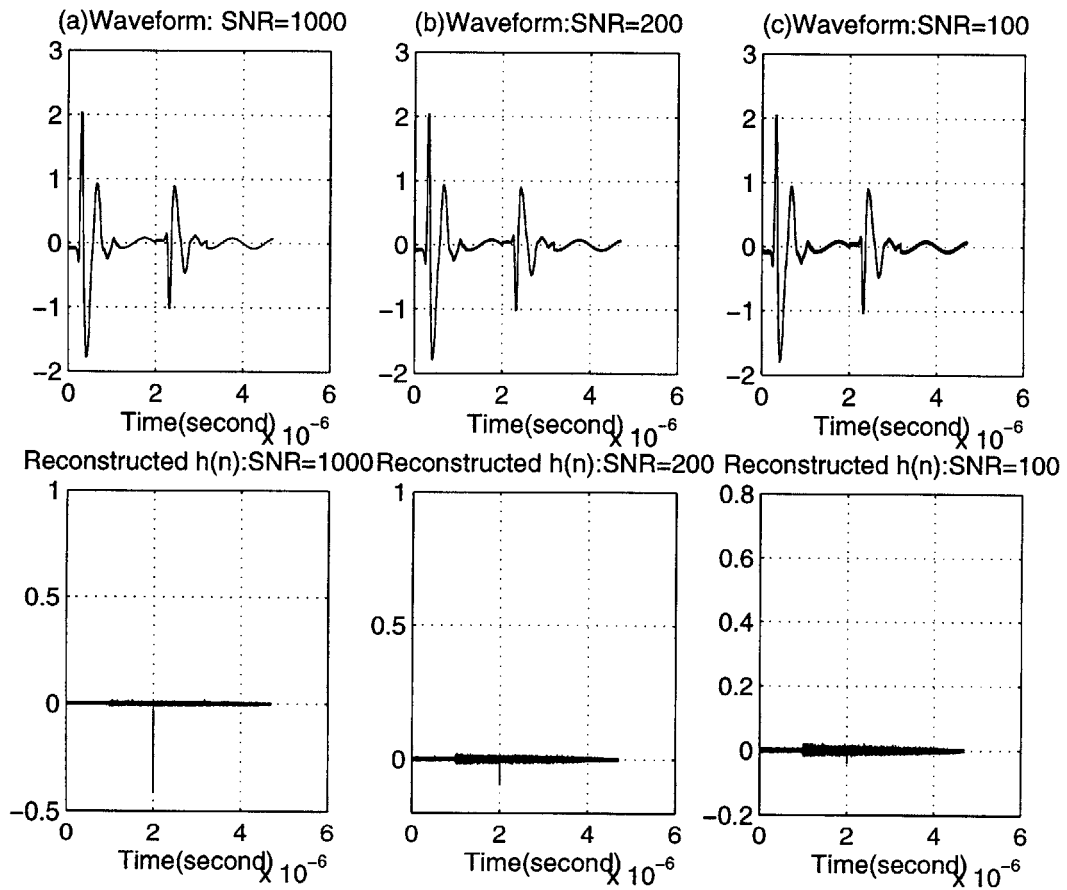


Figure 2.5: Deconvolution results with different noise level: (a) SNR=1000. (b) SNR=200. (c) SNR=100.

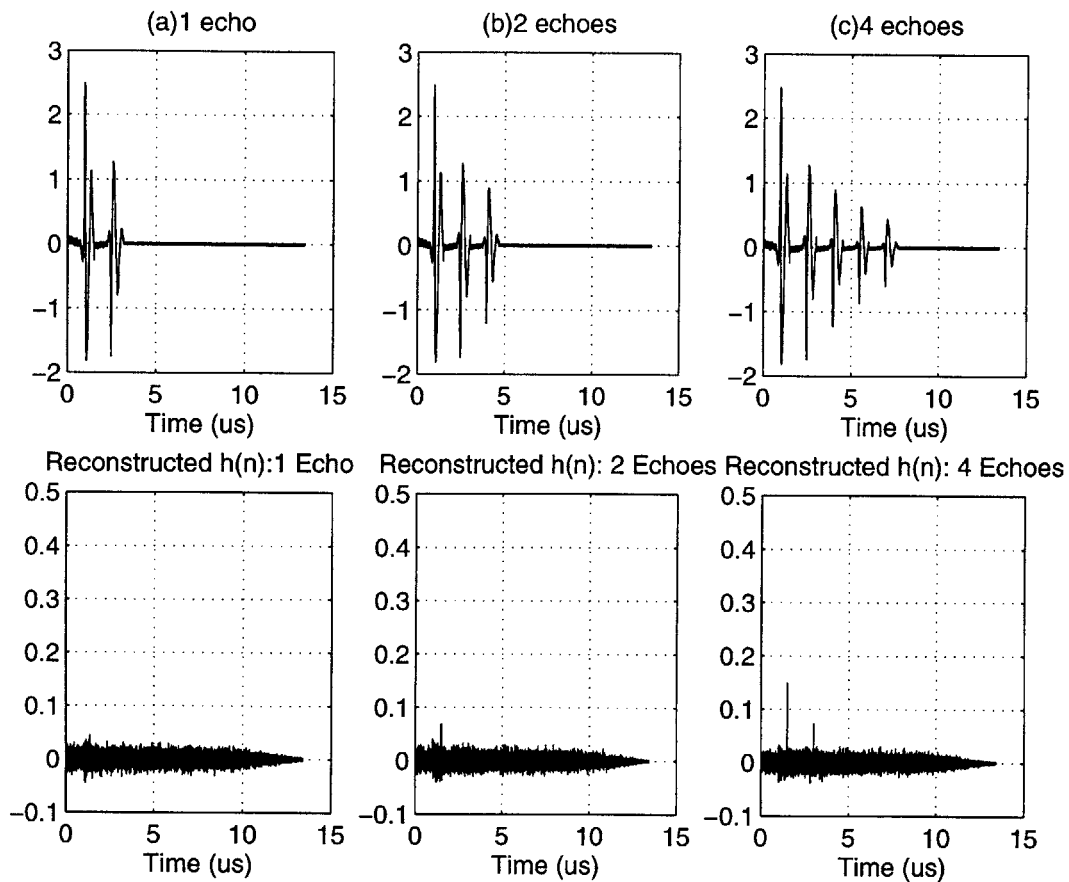


Figure 2.6: Deconvolution results with different number of echoes (SNR=150). (a) 1 echo. (b) 2 echoes. (c) 4 echoes.

application of this technique to echo detection. This also explains partially why this technique is still not widely used for ultrasonic signal processing even though it has the ability to give a perfect echo detection.

Number of Echoes

Figure 2.6 shows the effect of increasing the number of echoes. At the same noise level, the more echoes the signal contains, the better the deconvolution result will be. This has some practical implication in ultrasonic pulse-echo signal processing. By capturing a longer waveform, which could contain more echoes than a shorter waveform, better results are expected. However, a longer waveform requires more processing time and storage. Thus the trade-off should be well measured.

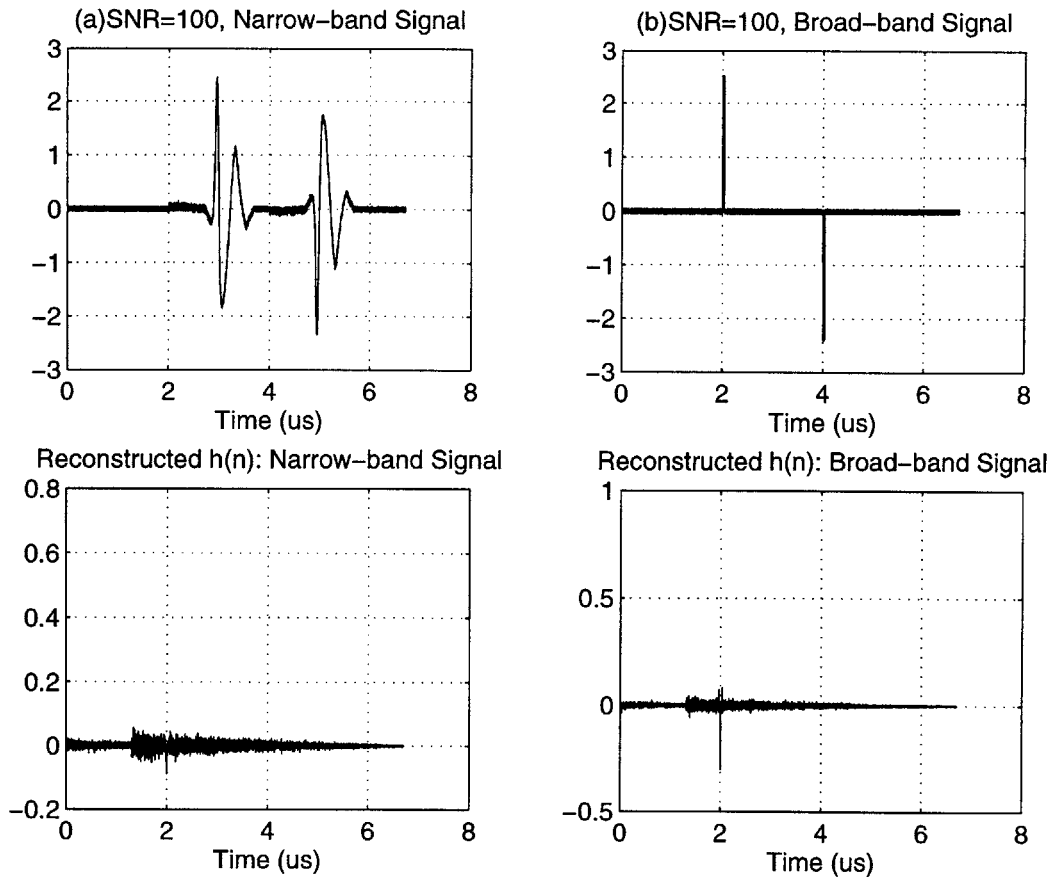


Figure 2.7: Deconvolution results: effect of bandwidth.

Bandwidth

To investigate the effect of the bandwidth of the basic pulse, two signals are synthesized. The first signal, shown in Fig. 2.7 (a), is obtained by convolving the basic pulse $x(t)$ with $h(t) = \delta(t) - 0.95\delta(t - 2\mu s)$. The second signal is obtained by replacing the basic signal with a rectangular pulse, as shown in Fig. 2.7 (b). The same amount of additive noise, with a SNR= 100, is added to both signals. Deconvolution results are shown in Fig. 2.7 (c) and (d). Deconvolving the first signal barely reveals the structure of $h(t)$ while $h(t)$ is clearly identified in the second case.

A comparison of the two pulses are shown in Fig. 2.8. The difference lies in the fact that a rectangular pulse has a much broader bandwidth than the basic pulse. This accounts for the difference in the deconvolution results.

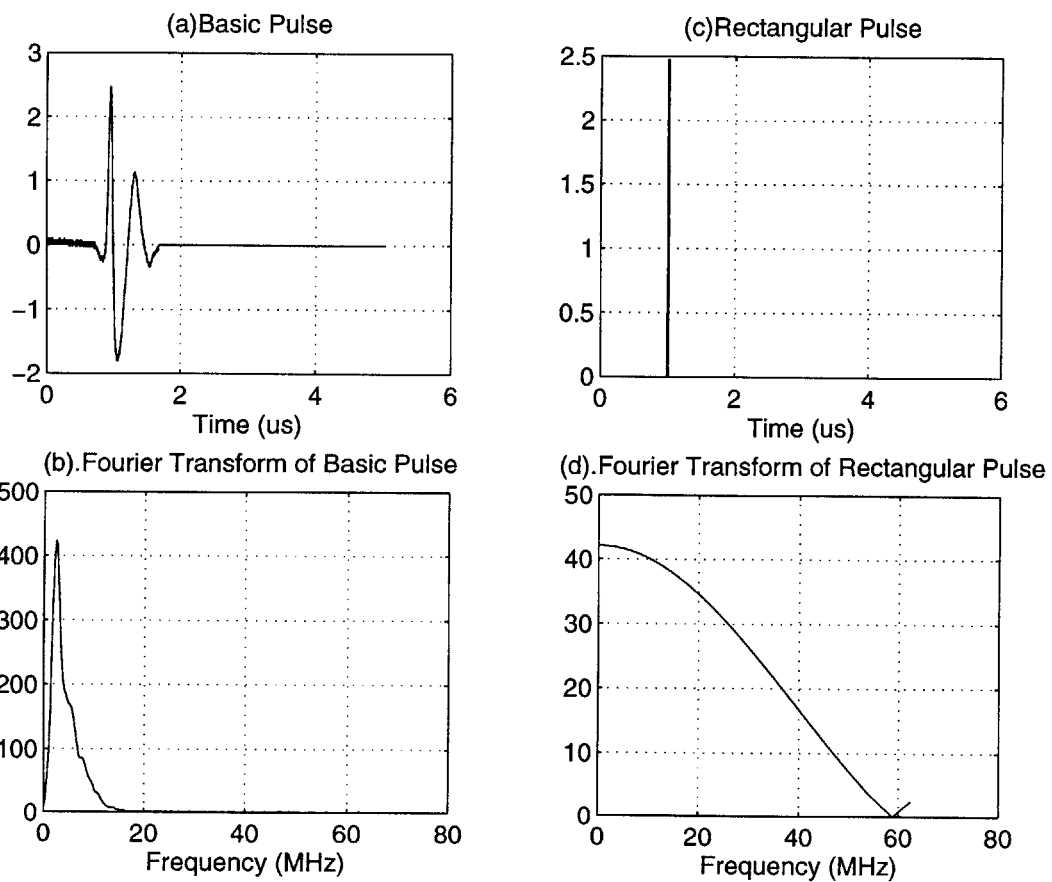


Figure 2.8: Comparison of the basic pulse and rectangular pulse.

As a conclusion, this deconvolution technique works better with broadband signals compared to narrow band signals. As a guideline for application, broadband transducers are preferred to narrow band transducers.

2.3 Summary

In summary of the above numerical studies, the following conclusions are drawn:

- When the signal is clean, cepstrum-based deconvolution technique is capable of providing perfect estimation of $h(t)$ without knowing $x(t)$.
- This technique is very sensitive to noise. It could fail even with very low noise level.
- Incorporating more echoes into the signal gives better deconvolution result.
- The cepstrum-based deconvolution technique performs better over broad band signals compared with narrow banded ones, which suggests a preference on broadband transducers.

These conclusions give insight into this signal processing technique and useful hints for experiments. Homomorphic deconvolution, although has good echo detection capability when the signal is clean, is too sensitive to noise to be applied to deconvolve real ultrasonic signals. Based on the above conclusions, a modified cepstrum-based deconvolution technique is proposed. This modified deconvolution technique is based on homomorphic deconvolution we discussed in this chapter, but it is more robust so that the noise contained in real experimental data doesn't cause failure to the application of the algorithm. It makes deconvolution of real ultrasonic experimental data feasible. Details of this modified deconvolution technique will be the topic of the next chapter.

Chapter 3

Modified Techniques for Ultrasonic Pulse-echo NDE of Layered Medium

This chapter discusses an ultrasonic pulse-echo detection model and proposes a signal processing technique based on traditional homomorphic deconvolution techniques. Due to the noise level in experimental data, traditional deconvolution techniques often fail in application. A modified deconvolution technique is proposed to address this issue. Experiments show that this modified cepstrum-based deconvolution technique works well in practice. Also, a post-processing technique to eliminate the by-product of the modified cepstrum-based deconvolution technique is suggested. Sample applications are demonstrated.

3.1 Ultrasonic Pulse-echo Signals

A typical ultrasonic pulse-echo setup is shown in Fig. 3.1. An ultrasonic transducer is used both as a transmitter and a receiver, either in contact or non-contact. In immersion testing, water is used as a coupling medium. The received waveform, which usually includes a main bang, and echoes from the front face, internal interfaces and backwall of the testing material (illustrated in Fig.3.2), contains rich information

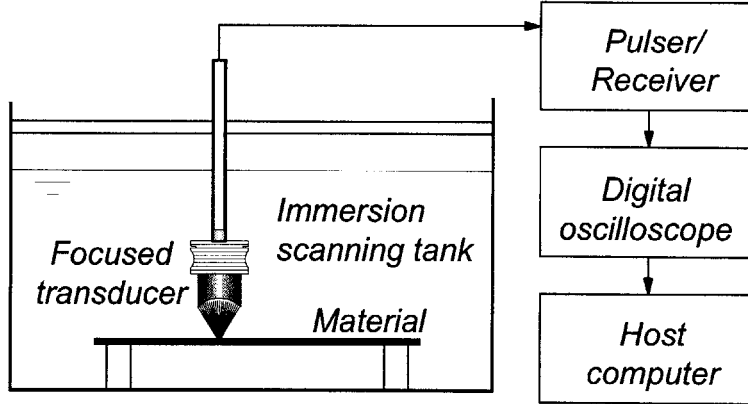


Figure 3.1: Ultrasonic pulse-echo experiment setup.

about the testing material. It is usually displayed on an oscilloscope and may be further digitized and stored in a host computer.

In brief, a received waveform, denoted by $y(t)$, can be modeled as the convolution of $x(t)$, frontface reflection of the ultrasonic pulse generated by the transducer, and the system function, $h(t)$. As a function of the testing material, $h(t)$ contains all the relative information about the material. We are interested in the investigation of the material, which normally involves estimating a part of or the complete $h(t)$:

$$y(t) = x(t) * h(t) , \quad (3.1)$$

where $h(t)$ is expressed in general as

$$h(t) = \sum_{i=0}^N a_i \delta(t - t_i) . \quad (3.2)$$

A multi-layer model is illustrated in Fig. 3.2, in which a testing sample is assumed to be of several layers immersed in water. Layer 1 is made of material 1, with a thickness of h_1 , a wave speed of c_1 . Likewise layer 2 is made of material 2, with a thickness of h_2 and a wave speed of c_2 , and so on. An ultrasonic pulse emitted from the transducer propagates into water first and then hits the interfaces between the layers: interface 1 (the interface between water and material 1); interface 2 (the interface

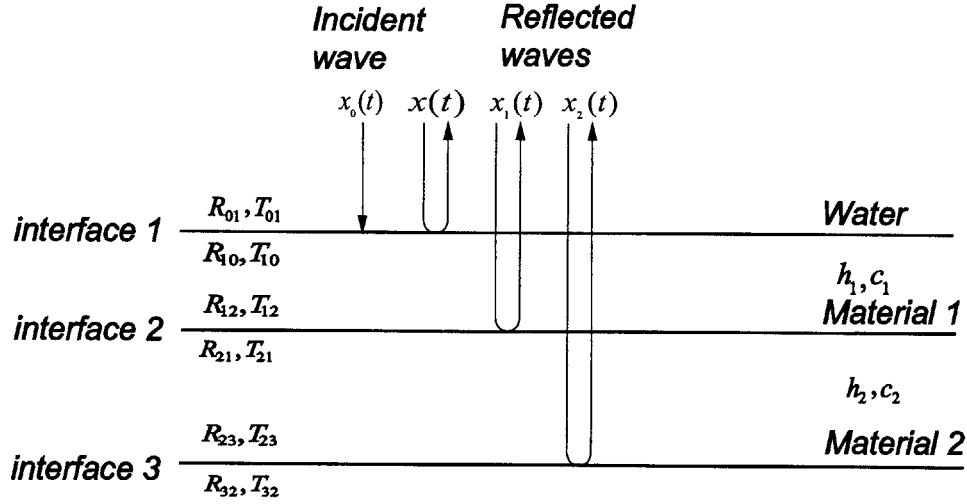


Figure 3.2: Ultrasonic wave propagation in a typical pulse-echo mode experiment.

between material 1 and material 2); interface 3 (the interface between material 2 and the material below material 2). *Reflection coefficients*, denoted by R_{xy} , are shown in the figure, where x represents the material that ultrasound comes from and y represents the material that ultrasound propagates into. For example, R_{01} represents the reflection coefficient when the wave is propagating from water into material 1. R_{10} denotes the reflection coefficient as the wave is propagating from material 1 into water. Similarly, *Transmission coefficients* denoted by T_{xy} are defined in a similar fashion. For instance, T_{12} represents the transmission coefficient of the amount of wave transmitting into materials 2 from material 1 and T_{21} represents the transmission coefficient in case that wave is propagating into material 1 from material 2, and so on.

A pulse generated by the transducer is denoted by $x_0(t)$. Similarly, $x(t)$ denotes the first reflection of $x_0(t)$ from interface 1, $x_1(t)$ represents the first reflection of $x_0(t)$ from interface 2 and $x_2(t)$ represents the first reflection of $x_0(t)$ from interface 3, which can be expressed for one-dimensional waves as:

$$\begin{cases} x(t) = R_{01}x_0(t - \frac{2h_0}{c_0}) \\ x_1(t) = T_{01}R_{12}T_{10}x_0(t - \frac{2h_0}{c_0} - \frac{2h_1}{c_1}) \\ x_2(t) = T_{01}T_{12}R_{23}T_{21}T_{10}x_0(t - \frac{2h_0}{c_0} - \frac{2h_1}{c_1} - \frac{2h_2}{c_2}) \\ x_3(t) = \dots \end{cases}$$

Solving for $x_0(t)$ from $x(t)$ and then substituting the corresponding result into the expressions of $x_1(t)$ and $x_2(t)$, we get:

$$\begin{cases} x_1(t) = \frac{T_{01}R_{12}T_{10}}{R_{01}}x(t - \frac{2h_1}{c_1}) \\ x_2(t) = \frac{T_{01}T_{12}R_{23}T_{21}T_{10}}{R_{01}}x(t - \frac{2h_1}{c_1} - \frac{2h_2}{c_2}) \\ x_3(t) = \dots \end{cases}$$

Defining

$$\begin{cases} a_1 = \frac{T_{01}R_{12}T_{10}}{R_{01}} \\ a_2 = \frac{T_{01}T_{12}R_{23}T_{21}T_{10}}{R_{01}} \\ t_1 = \frac{2h_1}{c_1} \\ t_2 = \frac{2h_1}{c_1} + \frac{2h_2}{c_2} \end{cases}$$

Equation (3.1) can be rewritten as:

$$\begin{cases} x_1(t) = a_1x(t - t_1) \\ x_2(t) = a_2x(t - t_2) \\ x_3(t) = \dots \end{cases}$$

The received signal can be written as:

$$y(t) = x(t) + x_1(t) + x_2(t) + x_3(t) + \dots \quad (3.3)$$

Substituting $x_1(t) = a_1x(t - t_1)$ and $x_2(t) = a_2x(t - t_2)$ into eq. (3.3), we get eq. (3.4):

$$y(t) = x(t) + a_1x(t - t_1) + a_2x(t - t_2) + \dots , \quad (3.4)$$

which can be rewritten as:

$$y(t) = x(t) * h(t) , \quad (3.5)$$

where:

$$h(t) = \delta(t) + a_1\delta(t - t_1) + a_2\delta(t - t_2) + \dots \quad (3.6)$$

In short, the received signal is a convolution of the front face reflection and a function $h(t)$, which is a simple function but contains all the information we are interested, such as wave speed, reflection coefficients, transmission coefficients, etc. We may define $h(t)$ as the system function. More precisely, it is the *system impulse response function*. In general, $x(t)$ is not limited to be the frontface reflection but from any interface. It is also possible to incorporate material attenuation in the model in a similar fashion.

As we know, the pulse-echo waveform contains rich both amplitude information and time-of-flight information. The above model, based on 1-D wave equations, gives insight into the relationship between the as-obtained waveform and material properties and thus lays the foundation for ultrasonic pulse-echo signal processing.

3.2 Difficulties in Applying the Homomorphic Deconvolution Technique

As shown in Chapter 2, cepstrum-based deconvolution is capable of fully recovering $h(t)$ from $y(t)$ without knowing $x(t)$. To this end, the cepstrum-based deconvolution technique discussed before seems to provide a good solution for measuring

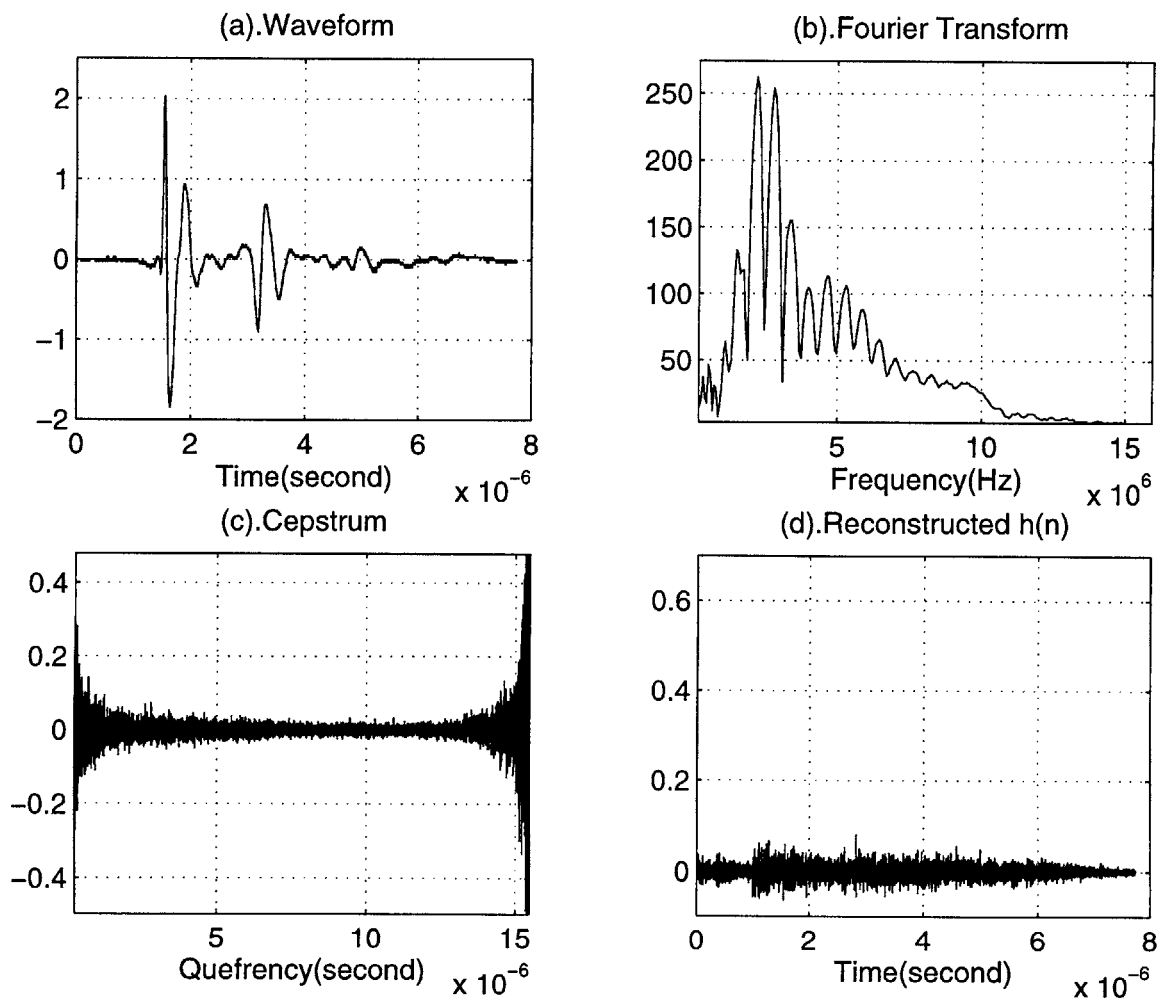


Figure 3.3: Cepstrum-based deconvolution procedure showing a failure in deconvolving a typical ultrasonic pulse-echo signal.

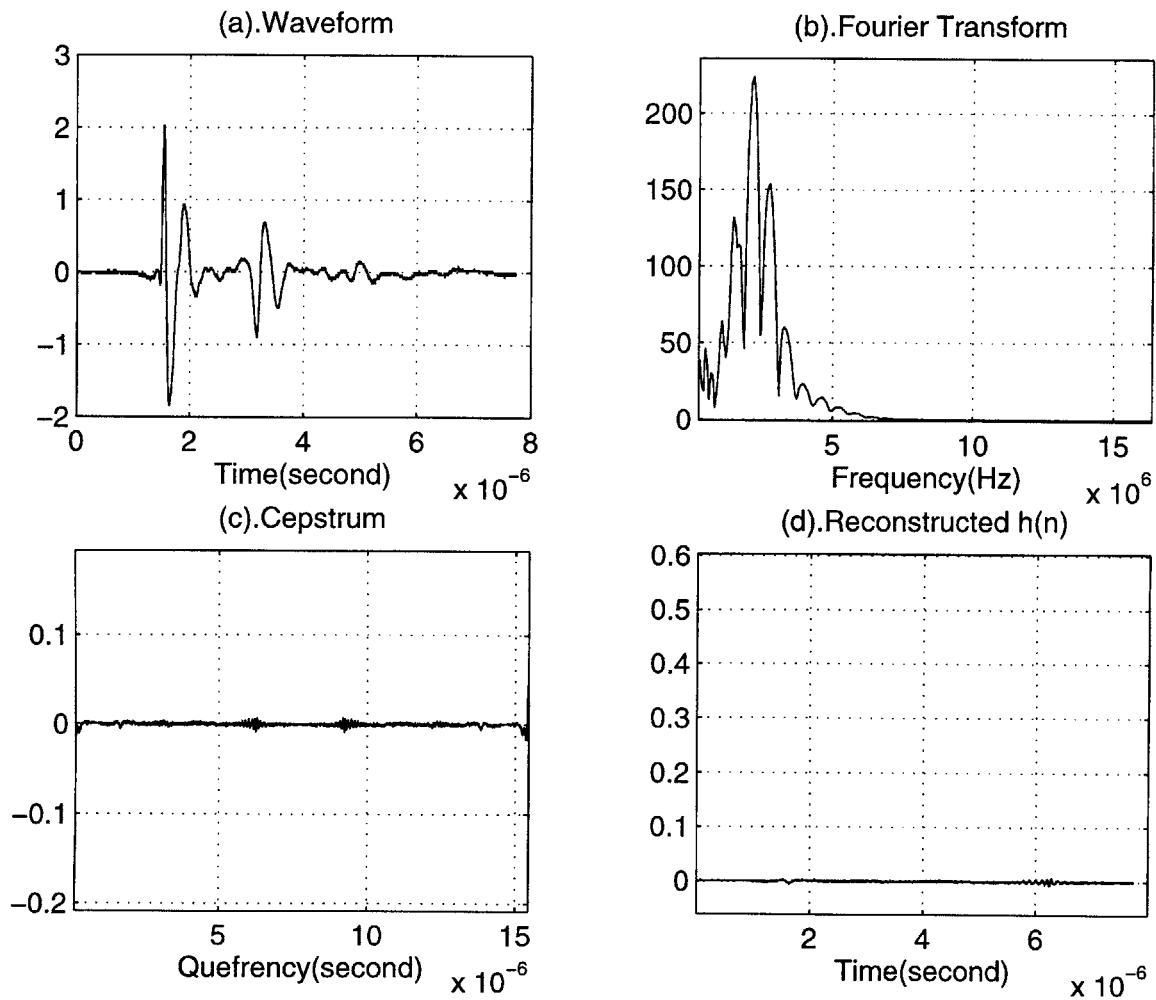


Figure 3.4: Deconvolution of the same signal in Fig. 3.3 after lowpass filtering.

time-of-flight. However, the sensitivity to noise of this technique very often leads its direct application into a failure.

Figure 3.3 is an example showing the deficiency of this deconvolution technique for deconvolving a signal obtained from a pulse-echo experiment for a composite laminate. Although there are two echoes clearly displayed in the time domain, deconvolution techniques failed, due to the sensitivity of the technique to noise as described in Chapter 2.

A useful technique for reducing the noise level is low-pass filtering. The signal in Fig. 3.3 was low-pass filtered with a cutoff frequency of 15 MHz and the corresponding

deconvolution result is shown in Fig. 3.4. Clearly there is some improvement: The cepstrum and the reconstructed signals are much smoother but still no echoes are detectable in the reconstructed $h(n)$. Further endeavor is needed in order to make the application of this deconvolution technique feasible.

3.3 Modified Deconvolution Technique

Figure 3.5 shows a proposed algorithm for ultrasonic pulse-echo signal processing. Instead of deconvolving the signal directly, we deconvolve the absolute value of the signal. It was shown in Chapter 2 that number of echoes contained in the signal has influence positively on the deconvolution results, i.e., more echoes result in better deconvolution efficiency under the same noise level. By taking the absolute value of the signal, we are actually increasing the number of echoes in the signal by creating artificial echoes in each pulse, normally by a factor larger than 3. This dramatic increase of number of echoes boosts the performance of the algorithm. We found that this modified deconvolution technique works well for all the ultrasonic pulse-echo signals we obtained from experiments.

Figure 3.6 shows the effect of taking the absolute value (a lowpass filter was applied before taking the absolute value): creating more echoes. Instead of the single pulse in Fig. 3.6(a), two extra echoes are created by taking the absolute value shown in Fig. 3.6(b) and they are detected in the deconvolved $h(n)$.

Figure 3.7 and Fig. 3.8 compare the performance of the two algorithms: the traditional deconvolution technique and the modified deconvolution technique. The same signal is used in both cases. Only the modified deconvolution technique detects echoes in the deconvolved $h(t)$.

Some important aspects of the algorithm are discussed in the followings:

Low-pass Filtering

Lowpass filtering is vital to the successful application of the algorithm due to the jaggedness of the raw data. This distortion caused by noise destroys the similarity

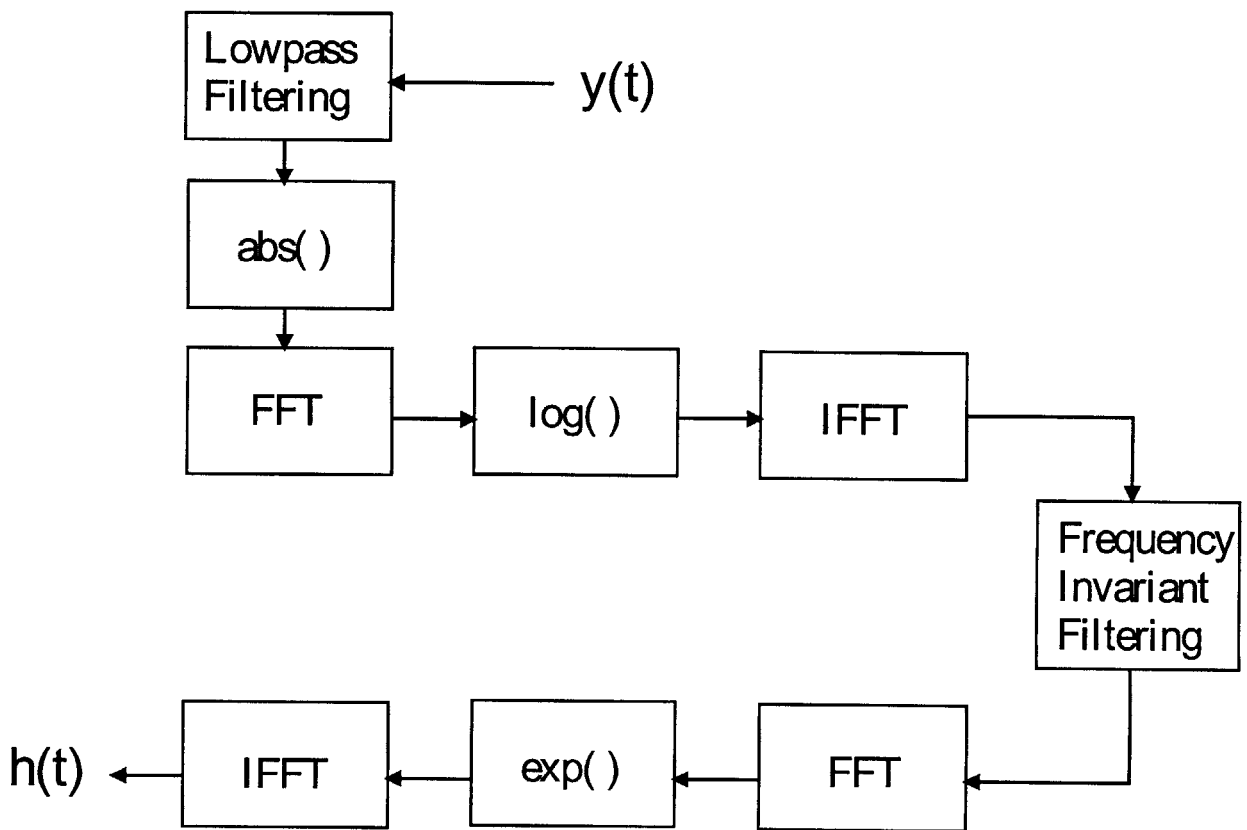


Figure 3.5: Modified cepstrum-based deconvolution procedure.

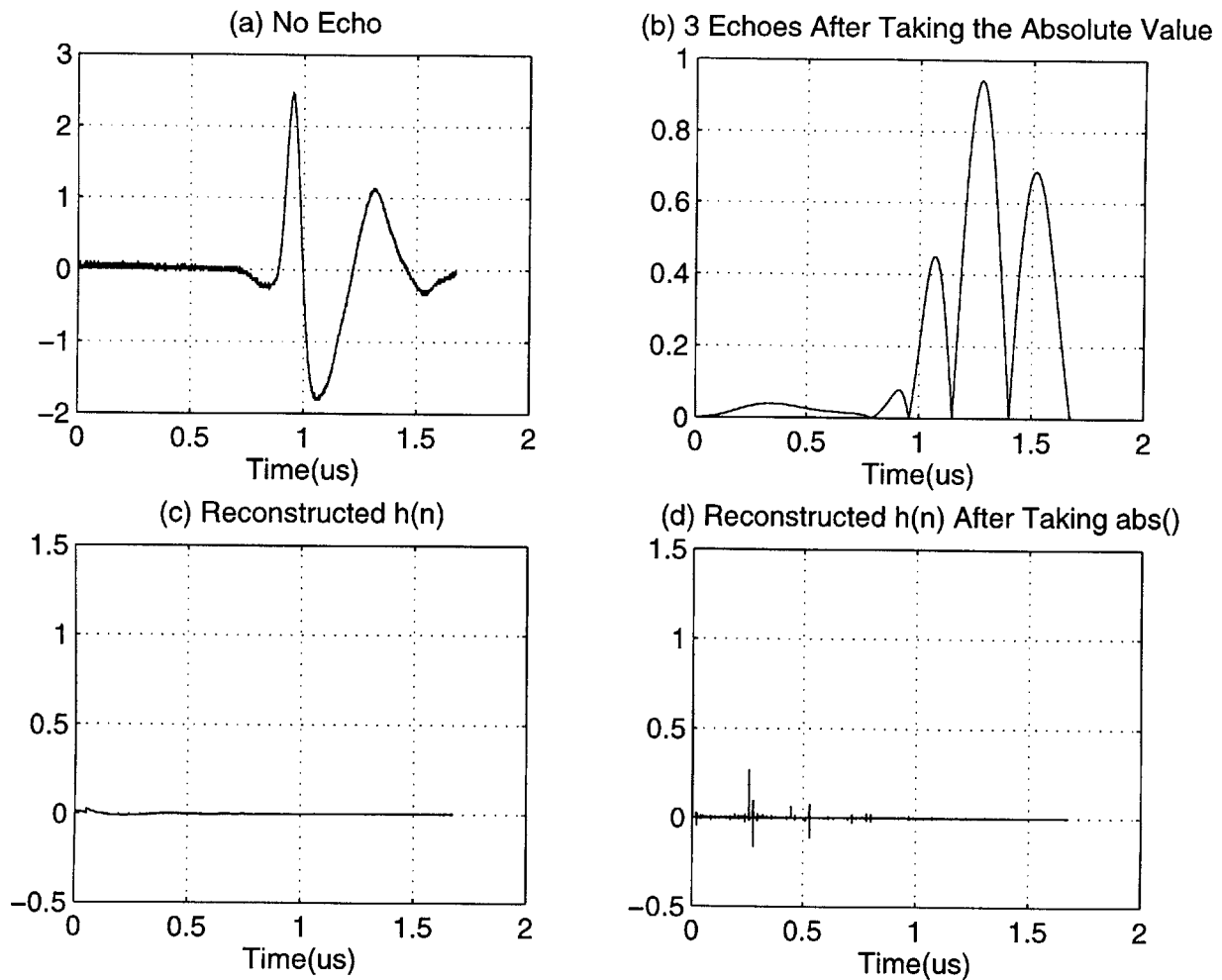


Figure 3.6: Creating more echoes by taking the absolute value.

between echoes. Without appropriate lowpass filtering, the lack of enough similarity between echoes will cause the algorithm to fail.

Cutoff frequency is the most important parameter in the design of a lowpass filter. The passband of the filter should cover at least the active band of the transducer. There is no rigorous formula to determine what is the best cutoff frequency. As a matter of fact, selection of the cutoff frequency is relatively flexible. In the case of using a 2.5 MHz broadband transducer, we found the a cutoff frequency between 15 MHz to 30 MHz gives a satisfying result.

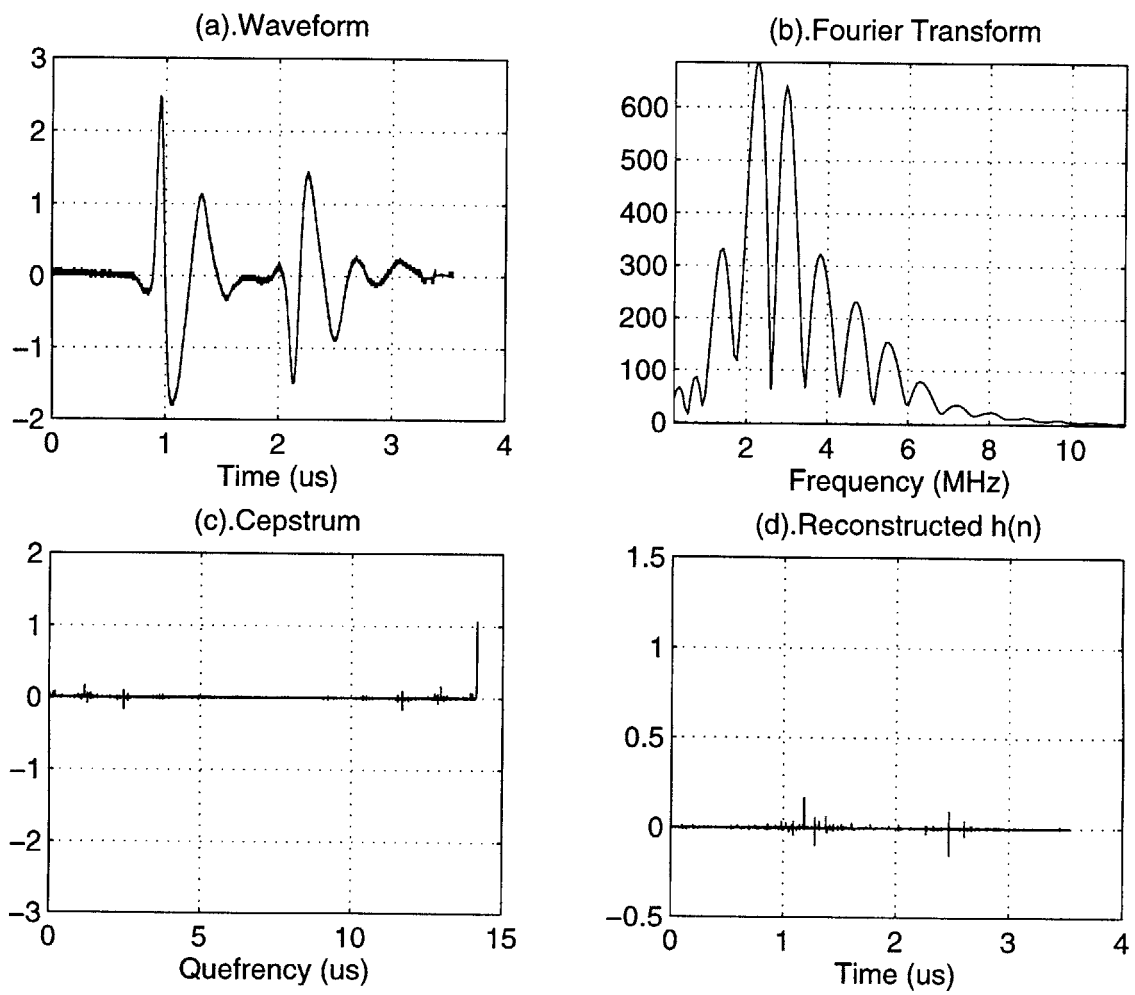


Figure 3.7: Deconvolution result from the modified deconvolution technique.

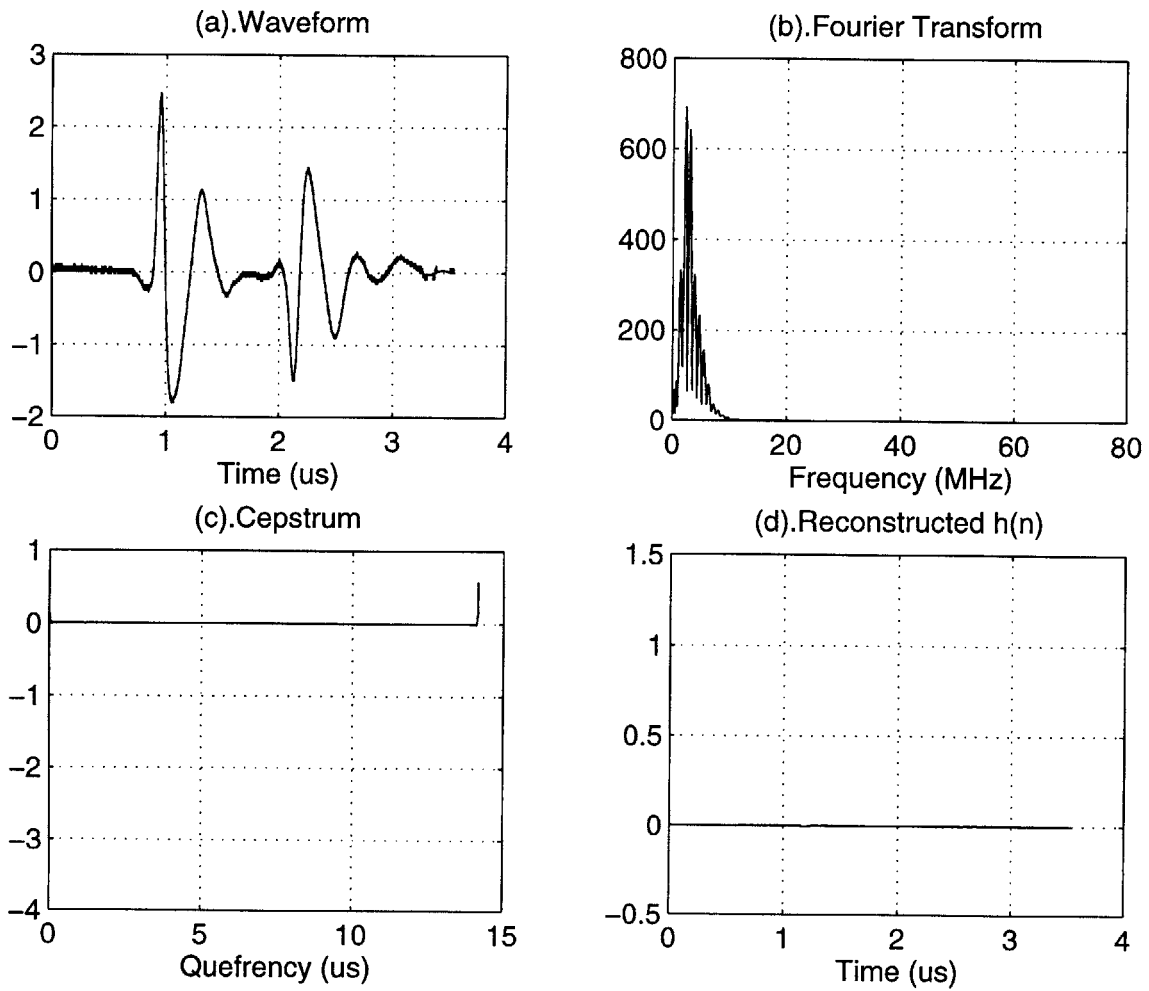


Figure 3.8: Deconvolution result from the traditional deconvolution technique.

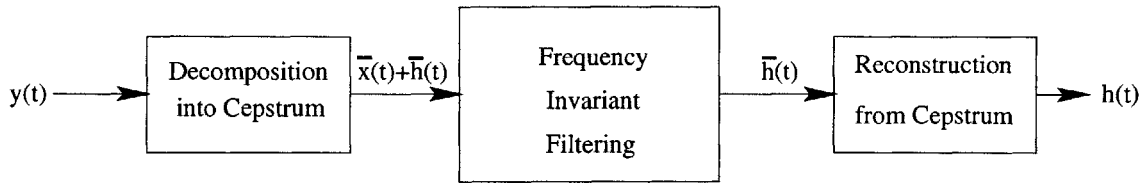
Frequency-Invariant Filtering in the Quefrequency Domain

The lowpass filter we mentioned in the above is called a *time-invariant filter*. A time-invariant system means that a time shift or time delay of the input sequence causes a corresponding shift in the output sequence. Specifically, suppose that a system transforms the input sequence $x[n]$ into the output sequence $y[n]$. The system is said to be time-invariant if for all n_0 the input sequence with value $x_1[n] = x[n - n_0]$ produces the output sequence $y_1[n] = y[n - n_0]$. A frequency-invariant system is defined in a similar way. This frequency-invariant filter plays a central role in the deconvolution process.

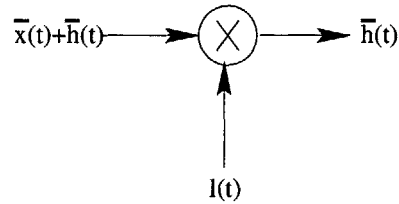
As discussed before, for the signal model in ultrasonic pulse-echo experiments, $y(t) = x(t) * h(t)$, $x(t)$ is the ultrasound pulse generated by an ultrasonic transducer and $h(t)$ is the system impulse response function of the testing material. $x(t)$ and $h(t)$ have different characteristics in the cepstrum domain. The cepstrum of $x(t)$, $\bar{x}(t)$, is concentrated in the neighborhood of zero quefrequency and decays fast as the quefrequency increases. The function $h(t)$ is more scattered over the whole cepstrum region. In other words, the ‘low-time’ portion of the cepstrum is mainly due to $x(t)$ and the ‘high-time’ portion is primarily due to $h(t)$. This suggests that the two convolved components of $y(t)$ can be separated by time gating, i.e., by frequency invariant linear filtering.

Figure 3.9 depicts the operations involved in separating the components of a convolution by frequency-invariant filtering. The frequency-invariant filter is often implemented by multiplication in the time domain (quefrequency domain) or by convolution in the frequency domain. Figure 3.10 (a) shows the time response of a lowpass frequency-invariant linear system as required for recovering an approximation to $x(t)$. Figure 3.10(b) shows the time response of a highpass frequency-invariant linear system for recovering an approximation to $h(t)$.

In our application, we are only interested in recovering $h(t)$ so that only the highpass filter is used. In the design of this highpass filter, cutoff quefrequency is the most important parameter. The selection of this cutoff time should make most of the

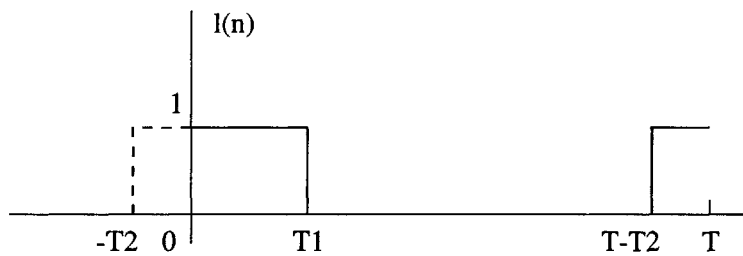


(a)

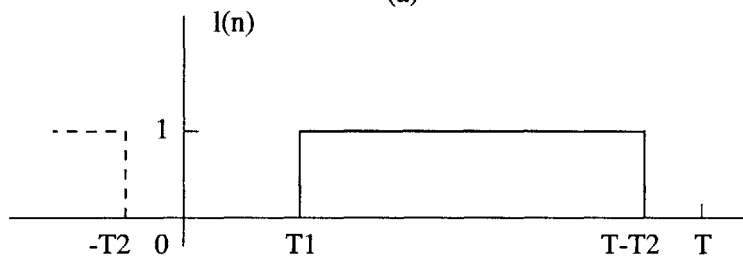


(b)

Figure 3.9: (a) System for homomorphic deconvolution. (b) Time-domain representation of frequency-invariant filtering.



(a)



(b)

Figure 3.10: Time response of frequency-invariant linear systems for deconvolution. (a) Lowpass system. (b) Highpass system. (Solid line indicates envelope of the sequence $l(t)$ as it would be applied in a DFT implementation. The dashed line indicates the periodic extension.)

energy of $\bar{h}(t)$ included in the passband while most of the energy of $\bar{x}(t)$ excluded from the passband. Since they are well-separated in the cepstrum, the cutoff quefrequency can be quite flexibly determined by considering the nearest possible echo to the frontface reflection that comes from the interface between the first layer and the second layer. An estimation of the time-of-flight, denoted by T_0 , for this echo can be obtained based on the estimation of the thickness of the first layer and wave speed. In the quefrequency domain, all the signals in the area of $t < T_0$, except for $t = 0$, are due to $x(t)$ whereas signals outside of $t < T_0$ could be due to either echoes or $x(t)$. Due to the fast decay rate of $x(t)$, we conclude that most of the energy of $x(t)$ resides in the area of $t < T_0$. Thus, setting a cutoff quefrequency t_1 close to T_0 but less than T_0 will bring the best separation effect without worrying about falsely filtering out echoes.

Post-processing

By taking the absolute value of the input signal, the robustness of the algorithm is increased and thus a better performance can be expected. However, this process creates additional artificial echoes, which also affect the deconvolved signal. In other words, the deconvolved $h(t)$ may contain not only the true echoes but also artificial ones, which are false and unwanted signals. It is necessary to eliminate this side-effect. An example is shown in Fig. 3.11.

From Figures 3.6 through 3.11, the following observations can be made:

- The spike with maximum amplitude corresponds to the true echo.
- Spikes representing false echoes are clustered. The cluster is centered or almost centered at the true echo. The number of spikes is equal to the number of oscillations in the single pulse.
- The space between two spikes are equal, which is approximately one half of the natural period of the transducer.

These observations are empirical but we found that they match well with experiments. Based on these observations, a post-processing procedure is developed as the follows:

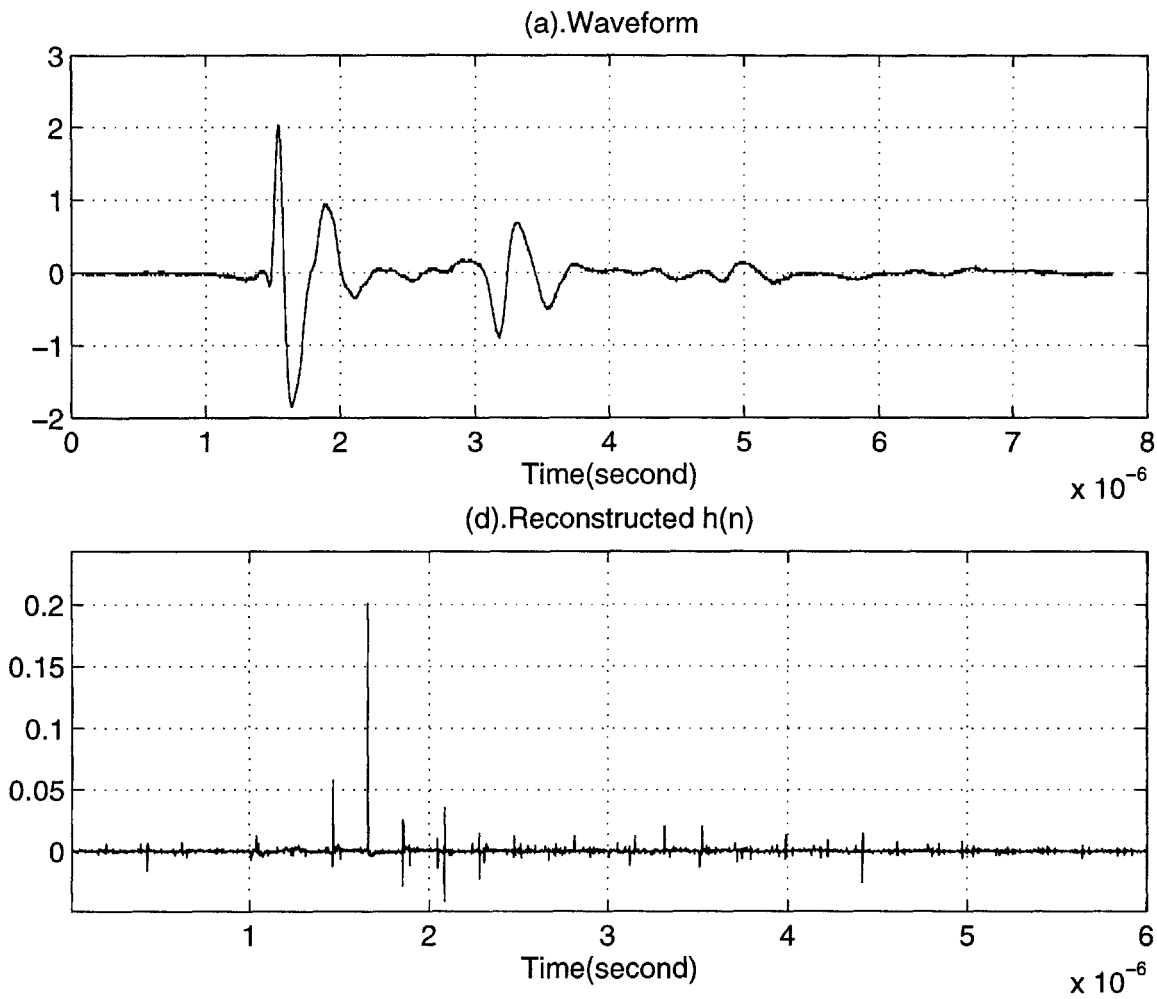


Figure 3.11: False echoes resulted from the modified deconvolution technique.

- Obtain the natural frequency of the transducer and count the number of ripples in the basic pulse.
- Calculate the time between adjacent artificial spikes, say T_0 , which is half the natural period of the transducer;
- Scan over the deconvolved $h(t)$, find significant local maxima (whose value is significantly larger than the other local values);

- For each significant local maximum, check the points at a distance of multiples of T_0 . Should a point exceed this local maximum, remove this local maximum and make it zero; Otherwise make all these points an amplitude of zero.

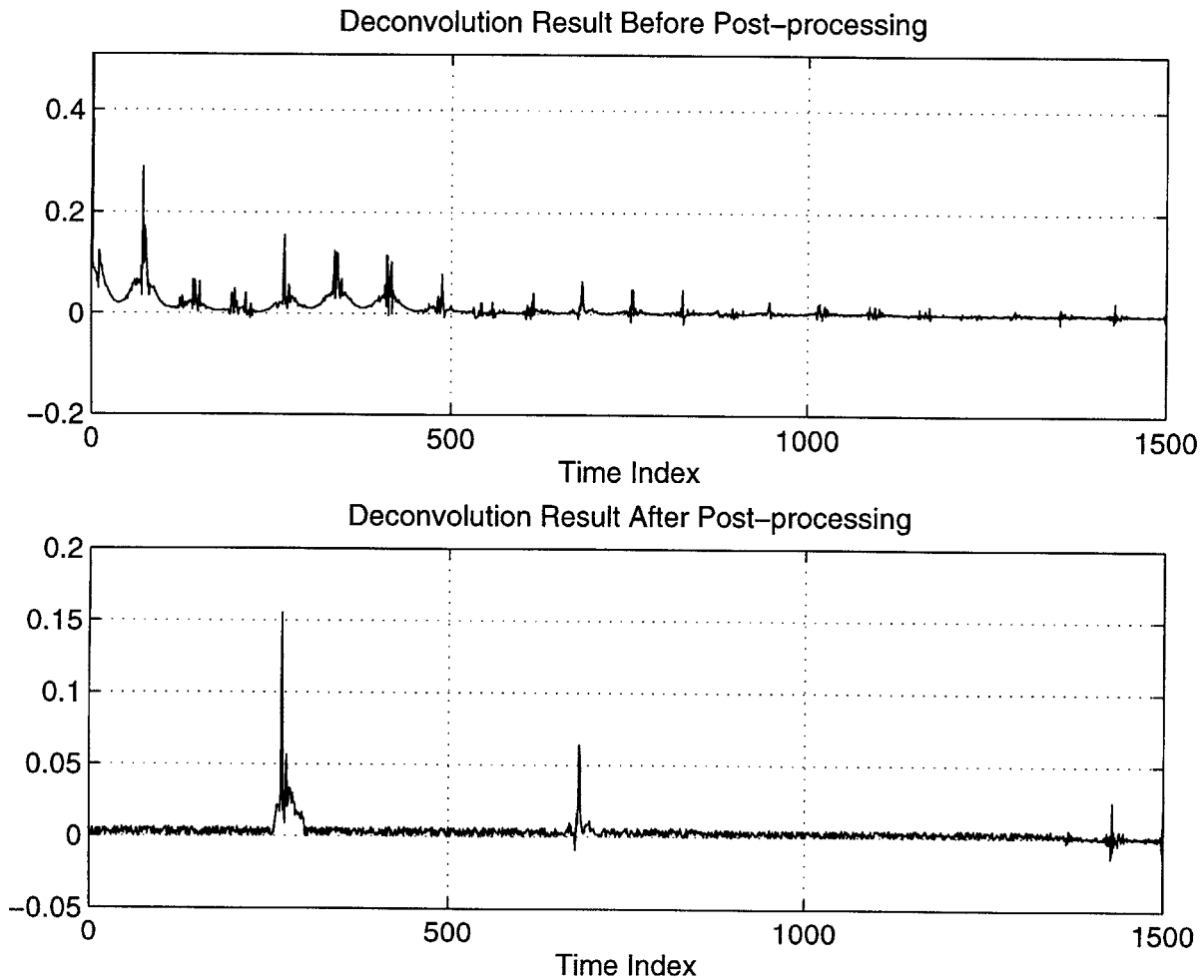


Figure 3.12: Post-processing for the modified cepstrum-based deconvolution technique.

Figure 3.12 shows the effect of applying the above post-processing technique to a signal obtained from a composite laminate. In the post-processed plot, the spike at time index 0 corresponds to the front face of the laminate; spikes at time indexes 268 and 681 are all indicators of delaminations located at these distances; The last spike at time index 1428 corresponds to the back face of the material.

3.4 Summary

Ultrasonic pulse-echo signal modeling and proposed signal processing techniques were discussed in this chapter. Due to the noise embedded in experimental data, traditional deconvolution technique often failed in application. A modified deconvolution technique is proposed to solve this problem. Experiences show that this modified cepstrum-based deconvolution technique works well in practice. Also, a post-processing technique to eliminate the by-product of the modified cepstrum-based deconvolution technique is suggested. Some sample applications are also shown.

Modified cepstrum-based deconvolution technique could not provide the full information of $h(t)$. It provides very good estimation of the time-of-flight of echoes. The time-of-flight information is of importance and sufficient for many ultrasonic NDE problems, such as ultrasonic imaging. In these applications, modified cepstrum-based deconvolution technique will be invaluable, which turned out to be a very good tool for measuring the time-of-flight. In the next chapter we will focus on the application of the proposed technique in ultrasonic imaging of composite laminates.

Chapter 4

Ultrasonic Imaging of Composite Laminates

Ultrasonic pulse-echo imaging is quite extensively used for detecting delaminations in composites. C-scan methods provide qualitative planar information. B-scans and three-dimensional scans (Woo and Daniel, 1994) can effectively determine the location of delamination in the thickness direction by measuring the time-of-flight between the echoes appearing in the A-scans. The time-of-flight measurements are usually done in the time domain using either a gated peak detector or numerically from digitized waveforms. The major drawback of the time-domain processing is that the signals reflected from interfaces have certain widths while the interfaces themselves have absolutely zero thickness. As a result of time-domain processing, in the B-scans, interfaces often appear falsely as thick lines. Furthermore, the technique provides poor measurement accuracy, particularly when the echoes overlap with each other. It is often advantageous to process the signal in the transform domain which allows highly flexible operations. This chapter focuses on application of the cepstrum-based deconvolution techniques for imaging flaws in composite laminates. Signal processing examples and sample images obtained from different signal processing techniques are shown.

4.1 Composite Materials

Composite materials generally offer significant practical and potential advantages over conventional materials in many critical structural components. The ever expanding structural application of composites expose themselves to various environmental and loading conditions, causing higher probability of induced damage in the material.

Thin laminated composite are usually susceptible to transverse loads. The mismatch in bending stiffness between the layers introduce large inter-laminar shear stresses even for quasi-isotropic laminates. As a result, inter-laminar delaminations may occur, which are detrimental to the performance of the structure. Dynamic loads such as low velocity impact loading may also introduce similar damage which may act as nuclei of further structural failure (ASTM STP, 1974). Consequentially, it is necessary to detect and characterize such defects nondestructively at an early stage of damage growth.

4.2 Experimental Setup

We fabricated 8-ply and 16-ply quasi-isotropic graphite/epoxy laminates (AS4/3501-6, Hercules) with embedded Teflon film patches to simulate delaminations. The layup of the 16-ply laminate was $[0/\pm 45/90]_{2s}$, where three patches were embedded as shown in Fig. 4.1. Teflon patch A was embedded between the 4th and 5th layers. Teflon patch B was embedded between 7th and 8th layers. Teflon patch C was embedded between 11th and 12th layers. We also obtained a 12-ply $[\pm 15_2/10_2]_s$ quasi-isotropic graphite/epoxy laminate with low velocity impact damage.

An immersion scanning system shown in Fig. 3.1 was used for acquiring A-scan data and imaging. A focused immersion transducer, with a center frequency of 2.5 MHz, was used to scan over the sample in a raster fashion using a mechanical positioning system. At each position, an ultrasonic pulse, $x(t)$, propagated into water and further into the composite material, whose returned echoes were received by the same transducer and recorded by a digital oscilloscope. The digitized waveforms were

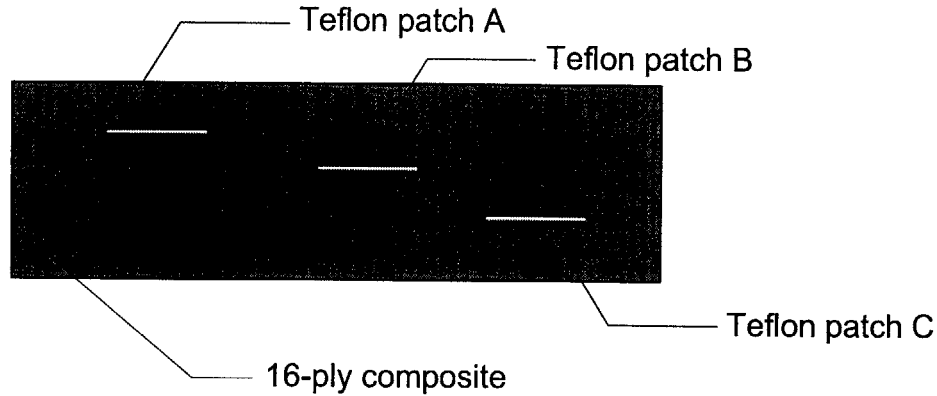


Figure 4.1: Schematic of a 16-ply composite laminate with Teflon patches embedded.

then transferred to the host computer and processed. The entire system, including mechanical scanning, digitization and data acquisition was centrally controlled by software residing in the host computer.

Figure 4.2 illustrates the reflections of ultrasound at different interfaces during the experiment.

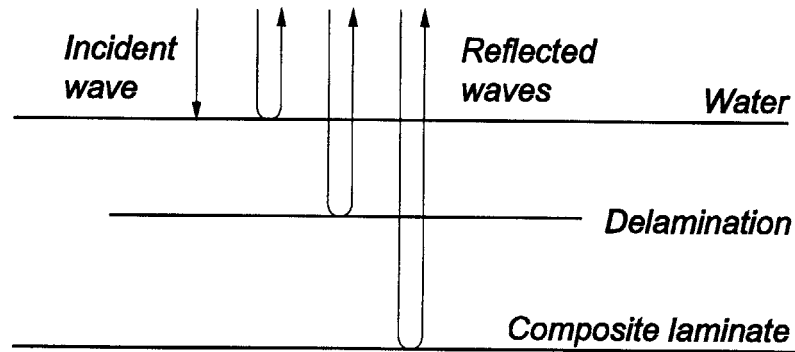


Figure 4.2: Reflection and transmission of ultrasound in material.

4.3 Processing of A-Scans

Typical A-scans are shown in Fig. 4.3. Figure 4.3(a) shows a waveform obtained at an area with no embedded patches. The first pulse corresponds to the front face of the material and the second echo represents the backface reflection. The waveform

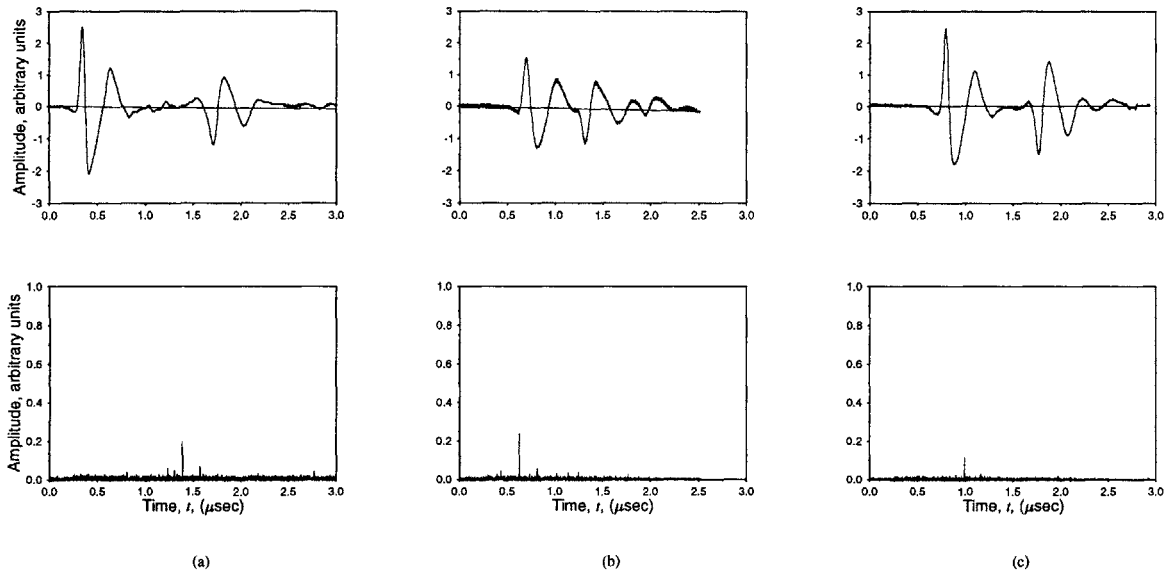


Figure 4.3: As-obtained waveforms using a transducer with a center frequency of 2.25 MHz and reconstructed signals after deconvolution for a 16-ply $[0/\pm 45/90]_{2s}$ quasi-isotropic graphite/epoxy laminate with embedded Teflon film patches: (a) Area with no embedded patches, (b) Teflon patch embedded between the 7th and 8th layers, (c) Teflon patch embedded between the 11th and 12th layers.

in Fig. 4.3(c) indicates the existence of an embedded Teflon patch, but the flaw is located far enough from the front face so that the echo does not overlap with the front face reflection. In these cases, it is relatively easy to obtain TOF by traditional time-domain signal processing techniques. But the waveform in Fig. 4.3(b) presents a much more challenging problem owing to the fact that reflected waves often interfere each other particularly when the interfaces are located closely. In this case, time-domain signal processing may fail while the cepstrum-based deconvolution technique is still capable of providing vital information.

In our experiments, all the A-scan waveforms are processed using the modified deconvolution technique as outlined before. It should be noted that lowpass filtering before taking the absolute value is of importance. With the transducer center frequency of 2.5 MHz, a cutoff frequency of 30 MHz was used.

The cutoff frequency of the frequency-invariant filter is also important. As discussed in Chapter 3, it was determined according to the estimated time-of-flight of reflection from the interface between layer 1 and layer 2. For example, if we estimate

that the time-of-flight is approximately $0.6 \mu\text{s}$, a cutoff frequency of $0.5 \mu\text{s}$ will be a good choice.

The post-processing technique discussed in chapter 3 was used to eliminate the artificial echoes introduced due to the rectification process.

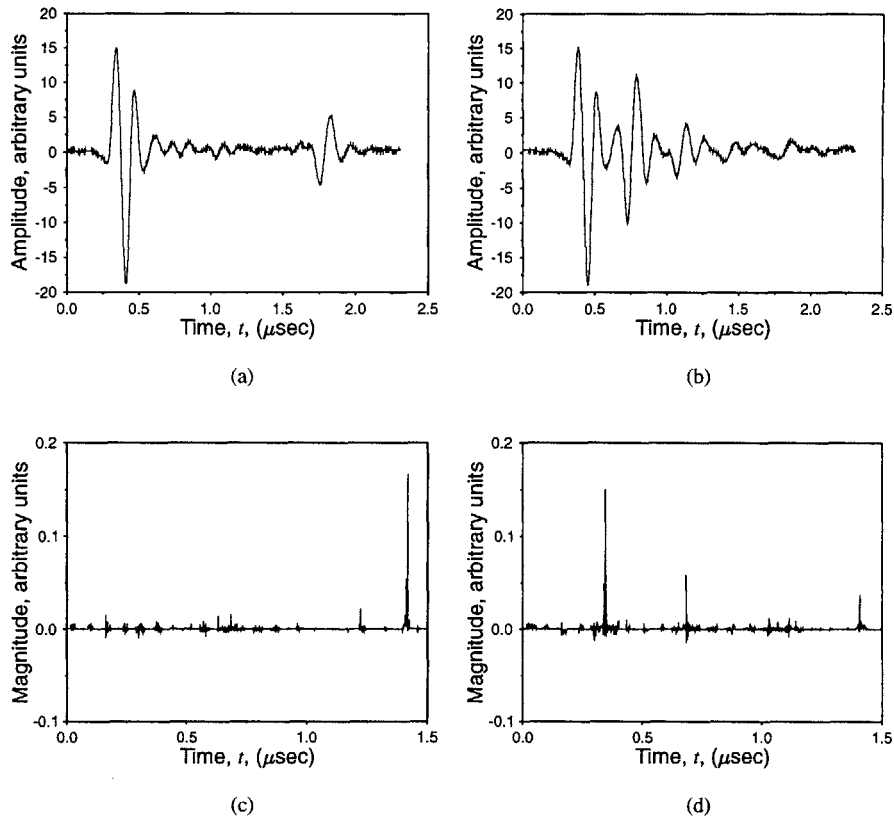


Figure 4.4: As-obtained waveforms using a focused transducer with a center frequency of 2.5 MHz and reconstructed signals after deconvolution for a 16-ply $[0/\pm 45/90]_{2s}$ quasi-isotropic graphite/epoxy laminate with embedded Teflon film patches: (a) Area with no embedded patches, (b) Teflon patches embedded between the 4th and 5th layers, (c) deconvolution result of the waveform shown in (a), (d) deconvolution result of the waveform shown in (b).

4.4 Results

Figure 4.3 shows the deconvolution results using the aforementioned technique. In Fig. 4.3(a), the first pulse is the reflection from the frontface of the composite plate and the second pulse is the reflection from the backwall. There is no defect at this location. The time-of-flight is about $1.45 \mu\text{s}$, which gives indication of the thickness of the plate. Fig. 4.3(b) shows the existence of Teflon patch B, embedded between the 7th and the 8th layers. The reflection from the Teflon patch is overlapped with the reflection from the front face and the reflection from the backwall is almost invisible due to the shadow effect, as shown in the waveform. Deconvolution correctly

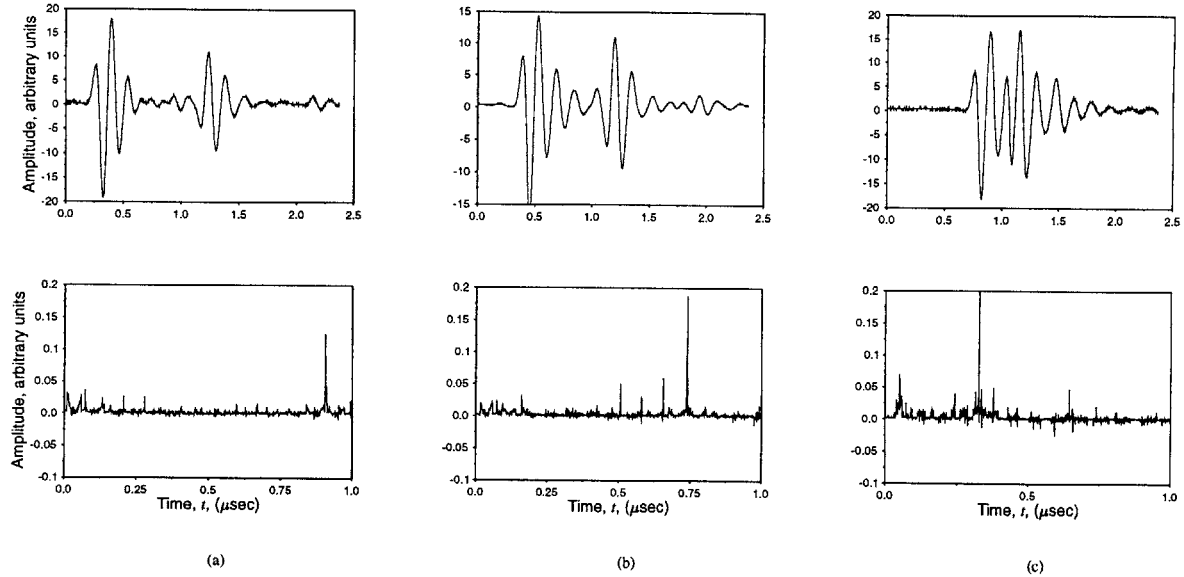


Figure 4.5: As-obtained waveforms and reconstructed signals after deconvolution for a 12-ply $[\pm 15_2/10_2]_s$ quasi-isotropic graphite/epoxy laminate with real impact damage : (a) Area with no impact, (b) area with impact damage, (c) Area with impact damage.

identified the location of the echo, approximately at $0.6 \mu\text{s}$. Fig. 4.3(c) detects an echo located at about $1.0 \mu\text{s}$, corresponding the location of Teflon patch C, embedded between the 11^{th} and the 12^{th} layers. Note here a transducer with a center frequency of 2.25 MHz is used.

Figure 4.4 compares the signals obtained from an area with no flaws and that of embedded patches. Teflon patch A was embedded between layer 4 and layer 5. Figure 4.4(d) correctly shows the time-of-flight from Teflon patch A to the front face to be about $0.35 \mu\text{s}$. Here a focused transducer with a center frequency of 2.5 MHz is used. Note the second largest spike in Fig. 4.4(d). This is due to *multiple reflections* instead of the occurrence of delamination at that location. This will be further discussed in the next chapter.

Signals and deconvolution results for real impact damaged specimen is shown in Fig. 4.5. The results from modified deconvolution technique clearly identified echoes and correspondingly delaminations due to low velocity impact damage.

Sample B-scan images are shown in Figures 4.6, 4.7, and 4.8. The specimen used is the 16-ply composite laminate with patches, as shown in Fig. 4.1. These figures are B-scan images of Teflon patch A, embedded between the 4th and the 5th layers, processed differently. Figure 4.6 is the result of the time-domain signal processing. Due to the oscillations contained in the ultrasonic pulse, a single interface with theoretically zero thickness is interpreted as a series of interfaces with an unacceptable thickness. Figure 4.7 was obtained by the modified cepstrum-based deconvolution technique without post-processing. An interface is correctly represented by a thin line in the image. However, a single interface is still misleadingly interpreted as a series of interfaces due to the artificial echoes created in the process. Post-processing removes this side-effect, as shown in Fig. 4.8.

4.5 Summary

Modified cepstrum-based deconvolution technique was applied to detect flaws in composite materials, including Teflon patches to simulate delaminations and real impact-damage. In the application, lowpass filtering, homomorphic filtering and post-processing are key factors considered.

Advanced composite material is gaining its significance recently due to its wide application in engineering systems. Its high performance and lightweight induce its important role for building up critical structural components, which necessitates NDE of composite material. For very thin layers, delamination maybe difficult to locate using ultrasound. The modified cepstrum-based deconvolution technique may provide a good solution to this problem.

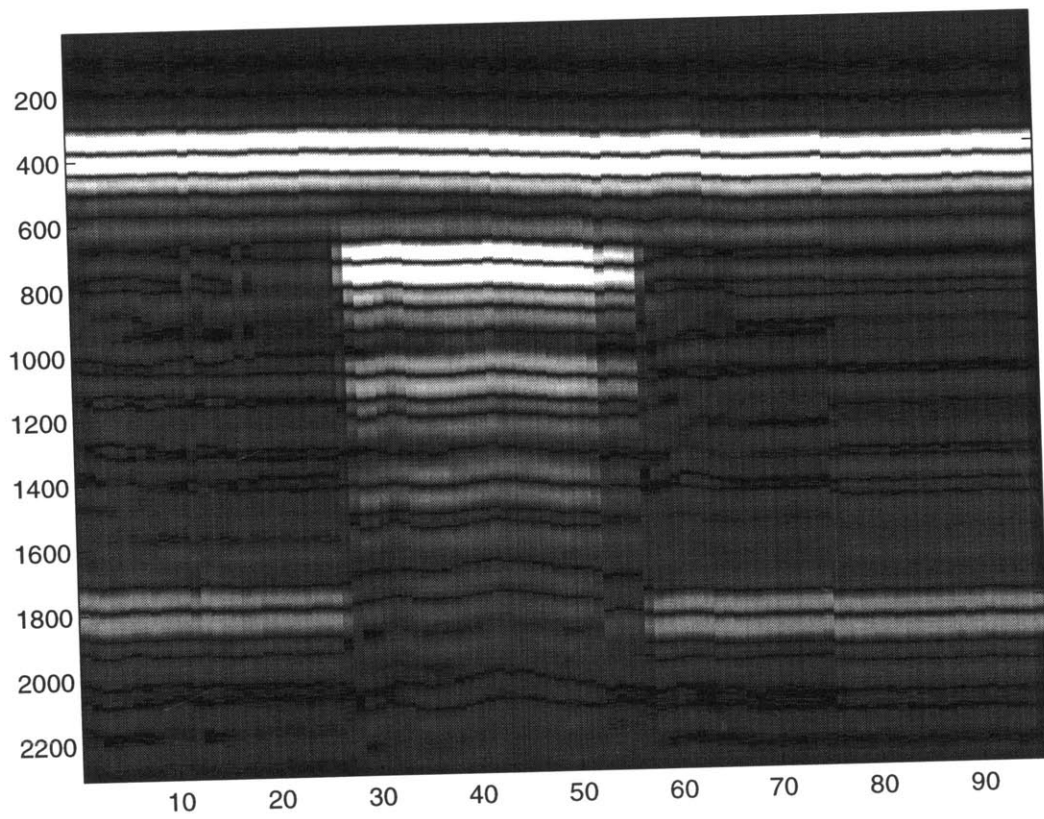


Figure 4.6: B-scan image of composite laminate with embedded Teflon patch. Time-domain processing.

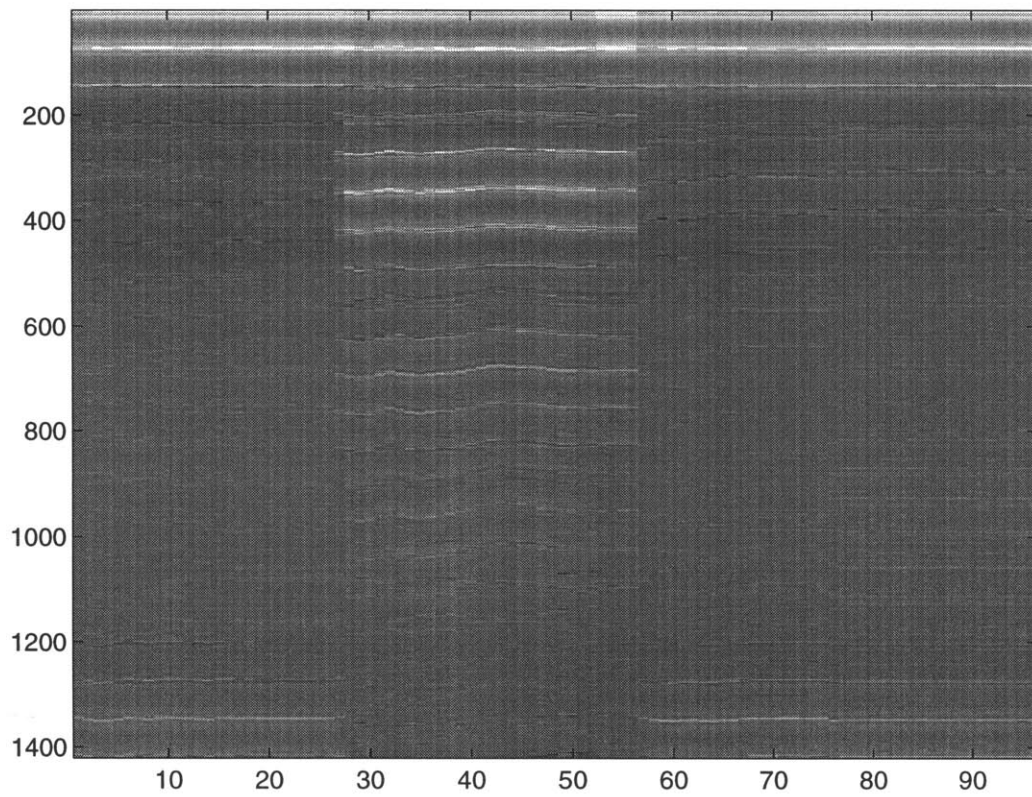


Figure 4.7: B-scan image of composite laminate with embedded Teflon patch. Modified cepstrum-based deconvolution technique without post-processing.

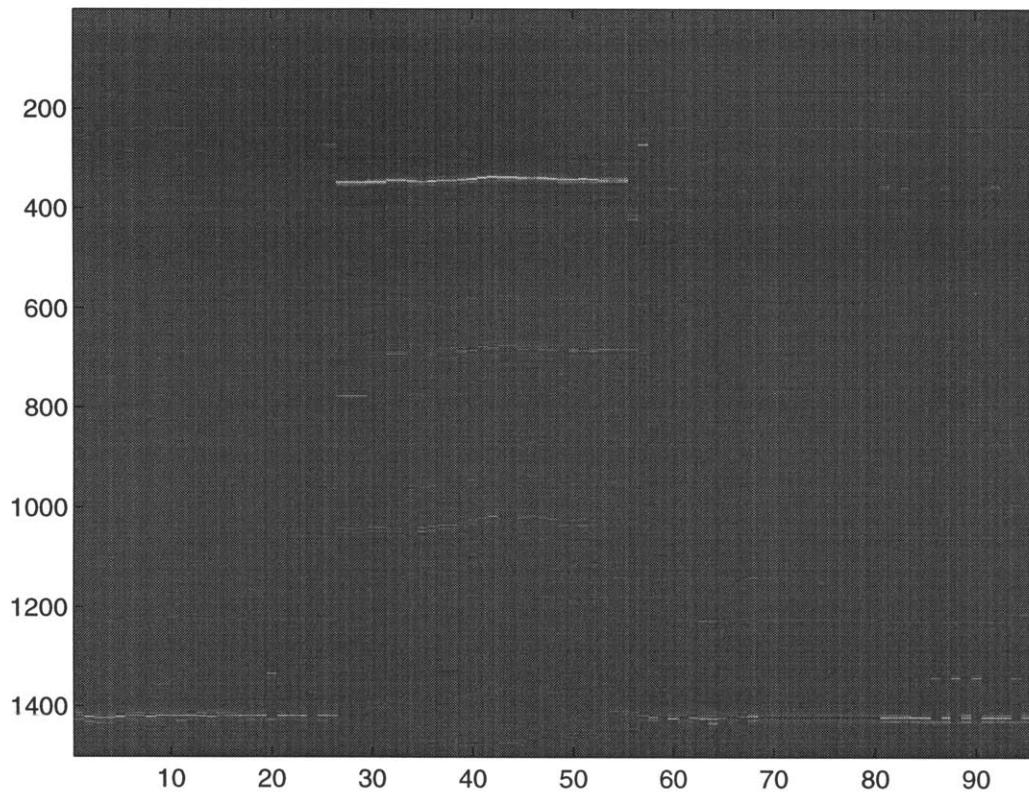


Figure 4.8: B-scan image of composite laminate with embedded Teflon patch. Modified cepstrum-based deconvolution technique after post-processing.

Chapter 5

Conclusion and Future Works

Ultrasonic imaging has been proven to be an effective and intuitive NDE method for characterizing flaws, for which various signal processing techniques have been successfully employed. However, poor resolution, dependence on operator's experiences and subjectivity in data interpretation have been hindering the wide acceptance of the technique of ultrasonic imaging.

Application of advanced composite materials signifies an important progress in structural engineering. Thereafter nondestructive evaluation of composite materials is brought up to the agenda of discussion. For thin layers, delaminations are difficult to locate using traditional time-domain signal processing techniques. Although successful in other applications, the thin layered structure of composite materials imposes a major challenge to them and thus shows a stronger demand for advanced signal processing techniques. For composite laminates, B-scan images obtained using these signal processing techniques are misleading in both sizing and locating delaminations.

An advanced signal processing technique, named as *the modified cepstrum-based deconvolution technique combined with post-processing*, was proposed in this thesis. After the demand for advanced signal processing is identified, a numerical study on homomorphic deconvolution was carried out. Homomorphic deconvolution has been successfully applied in other areas for years. Due to its sensitivity to noise level, we

find it often fails in deconvolving ultrasonic pulse-echo signals. Numerical experiments lead us to the following conclusions on homomorphic deconvolution:

- When the signals are clean, cepstrum-based deconvolution technique is capable of providing good estimation of $h(t)$ without knowing $x(t)$.
- The technique is very sensitive to noise, even at a very low level.
- Incorporating more echoes into the signal gives better deconvolution efficiency.
- The cepstrum-based deconvolution technique performs better for broad band signals compared to narrow banded signals, which suggests a preference on broadband transducers.

Instead of deconvolving the ultrasonic pulse-echo signal directly, we deconvolve the absolute value of the signal to create more echoes and thus increase the effectiveness of echo detection. Experiments show that this technique is effective for time-of-flight estimation. However, a post-processing procedure is needed due to the artificially introduced echoes. We proposed a post-processing technique based on numerical observations and it is shown to be effective in practice.

The above signal processing technique is successfully applied to ultrasonic imaging of composite laminates. A 16-ply composite plate has been fabricated with embedded Teflon patches to simulate delaminations. Using the proposed technique, we could precisely locate the location of Teflon patches from the obtained A-scan waveforms. B-scan image constructed by this technique clearly identified the location and size of the embedded Teflon patch and eliminated the problems associated with time-domain signal processing techniques. Real impact damaged composite specimen has also been investigated using this technique and delaminations caused by low velocity impact are also successfully located.

In summary, the following conclusions were made:

Time-domain signal processing techniques are capable of providing evidence of the existence of defects, but incapable of pinpointing the defect and sizing the defect. Modified deconvolution technique is capable of pinpointing the defect and sizing the

defect, but it gives false indications of delaminations due to the side-effect involved in the algorithm. Post-processing technique eliminates this problem successfully. The modified deconvolution technique with post-processing signifies an advancement in ultrasonic imaging of composite materials.

Several issues may be considered into future work, as outlined in the followings:

Multiple Reflections

Figure 4.4 shows the problem caused by multiple reflections. The second largest spike in the deconvolution result is not due to a delamination located at that location but due to the multiple reflections of the basic pulse between the front face and the delamination corresponding to the first large spike.

The same problem also appears in Fig. 4.8. How to eliminate this problem remains a question for further research.

Shadow Effect

In Fig. 4.8, the backwall is shadowed by the Teflon patch so that it disappeared in the image. This is due to the *shadow effect*. For multiply stacked delaminations, one may hide the others so that some of them may not be seen in the obtained image. Shadow effect is due to the physical law and more advanced processing techniques may be required to reduce the influence of this effect.

Post-processing Technique

Post-processing technique is of great importance to the successful application of the modified cepstrum-based deconvolution technique to ultrasonic imaging. The proposed post-processing technique is empirical. Although it worked well in our experiments, it is not guaranteed that it will work well in other experiments. Thus, an effective and reliable post-processing technique will be necessary in future works.

Bibliography

1. ASTM STP (1974), "Foreign object impact damage to composites," *American Society for Testing and Materials*, Philadelphia, PA.
2. Bogert, B. P., Healy, M. J. R., Tukey, J. W. (1963), "The quefreny analysis of time series for echoes: cepstrum, pseudo-autocovariance, cross-cepstrum, and saphe cracking," *Proc. Symposium Time Series Analysis*, M. Rosenblatt, Ed., John Wiley and Sons, New York, pp 209-243.
3. Chang, F.H., Couchman, J.C., and Yew, B.G.W. (1971), "Ultrasonic Resonance Measurements of Sound Velocity in Thin Composite Laminates," *Journal of Composite Materials*, Vol.8, 1974, pp 356-363.
4. Daniel, I. M., and Ishai, O. (1994), "Engineering Mechanics of Composite Materials," Oxford University Press, New York.
5. Daniel, I. M., and Wooh, S. C. (1990), "Deformation and damage of composite laminates under impact loading," *Impact Response and Elastodynamics of Composites*, ASME AMD-Vol. 116, eds. A.K.Mal and Y.D.S.Rajapakse, 11-26.
6. Finn, S. R., He, Y. F., and Springer, G. S. (1993), "Delaminations in composite plates under transverse impact loads—experimental results," *Composite Structures*, Vol. 23, pp 191-204.
7. Iyer, V.R., and Kinra, V.K. (1991a), "Frequency domain ultrasonic measurement of the thickness of a sub-half-wavelength adhesive layer," *Proceedings of the 1991 SEM Spring Conference on Experimental Mechanics*, Milwaukee, Wisconsin, 1991, pp 668-675.
8. Iyer, V.R., and Kinra, V.K. (1991b), "Characterization of a sub-half-wavelength adhesive layer using ultrasonic spectroscopy," *Enhancing Analysis Techniques for Composite Materials*, ASME-NDE, Vol.10, 1991, L. Schwer, J.N. Reddy, and A.K. Mal, eds., pp 35-41.

9. Jessop, T. J., P. J. Mudge and J. D. Harrison (1989), *Ultrasonic Measurement of Weld Flaw Size*, Transportation Board, Report No. 242, Dec. 1989.
10. Kinra, V.K., and Dayal, V. (1988), "A new technique for ultrasonic NDE of thin specimens," *Experimental Mechanics*, Vol.28, No.3, 1988, pp 288-297.
11. Krautkämmer, J. and Krautkrämer, H. (1990), *Ultrasonic Testing of Materials*, 4th ed., Springer-Verlag, New York.
12. Mak, D. K. (1985), "Ultrasonic methods for measuring crack location, crack height, and crack angle," *Ultrasonics*, September, 223-226.
13. Ogura, Y. (1983), "Height determination studies for planar defects by means of ultrasonic testing," *The Non Destructive Testing Journal, Japan*, 1(1), 22-29.
14. Oppenheim, A. V. and Schafer, R. W. (1991), "Discrete-time signal processing," Prentice Hall, Englewood Cliffs, NJ.
15. Oppenheim, A. V. (1969), "A speech analysis-synthesis system based on homomorphic filtering," *J. Acoustical Society of America*, Vol. 45, Feb., pp 458-465.
16. Pialucha, T., Buyott, C.C.H., and Cawley, P. (1989), "An amplitude spectrum method for the measurement of phase velocity," *Ultrasonics*, Vol.27, 1989, pp 270-279.
17. Reut, Z., Pace, N. G., and Heaton, M. J. P. (1985), "Computer classification of Sea Beds by Sonar," *Nature*, Vol. 314, April, pp 426-428.
18. Schafer, R. W., and Rabiner, L. R. (1970), "System for automatic formant analysis of voiced speech," *J. Acoustical Society of America*, Vol. 47, No. 2, Pt.2, Feb., pp 634-648.
19. Senmoto, S., and Childers, D. G. (1972), " Adaptive decomposition of a composite signal of identical unknown wavelets in noise," *IEEE Trans. on Systems, Man, and Cybernetics*, Vol. SMC-2, No. 1, Jan., p. 59.
20. Tribolet, J. M. (1979), "Seismic applications of homomorphic signal processing," Prentice Hall, Englewood Cliffs, NJ.
21. Ulrych, T. J. (1971), "Application of homomorphic deconvolution to seismology," *Geophys.*, Vol. 36, No. 4, August, pp 650-660.
22. Wooh, S. C., and Daniel, I. M. (1994), "Three-dimensional ultrasonic imaging of defects and damage in composite materials," *Materials Evaluation*, Vol. 10, pp 1199-1206.

23. Wooh, S. C. (1995), "Role of NDE in civil infrastructure condition assessment'," present and future, Keynote Lecture, *International Workshop for Application of NDT Technology for Failure Prevention*, Jointly organized by Korean Society for Nondestructive Testing (KSNT) and Research Institute of Mechanical Technology (RIMT) of Pusan National University, Oct. 18–20.